Osteoporotic bone loss from excess iron accumulation is driven by NOX4-triggered ferroptosis in osteoblasts

Hui Zhang
Second Affiliated Hospital of Soochow University
Aifei Wang
Second Affiliated Hospital of Soochow University
Guangfei Li
Second Affiliated Hospital of Soochow University
Qiaocheng Zhai
Soochow University Medical College
Zhengyun Huang
Soochow University Medical College
Xiao Wang
Second Affiliated Hospital of Soochow University
Zihou Cao
Second Affiliated Hospital of Soochow University
Lulin Liu
Second Affiliated Hospital of Soochow University
Gongwen Liu
Suzhou TCM Hospital Affiliated to Nanjing University of Chinese Medicine: Suzhou Hospital of Traditional Chinese Medicine
Bin Chen
Second Affiliated Hospital of Soochow University
Keyu Zhu
Second Affiliated Hospital of Soochow University
Ying Xu
Soochow University Medical College
Youjia Xu (xuyoujia@suda.edu.cn)
Second Affiliated Hospital of Soochow University https://orcid.org/0000-0002-9826-4324

Research Article

Keywords: ferroptosis, osteoporosis, iron, osteoblast, GPX4, NOX4

Posted Date: July 1st, 2022

DOI: https://doi.org/10.21203/rs.3.rs-1749712/v1

Abstract

Excess iron accumulation is a risk factor for osteopenia and osteoporosis, and ferroptosis is becoming well understood as iron-dependent form of cell death resulting from lipid peroxide accumulation. However, any pathological impacts of ferroptosis on osteoporosis remain unknown. Here, we show that ferroptosis is involved in excess-iron-induced bone loss and demonstrate that osteoporotic mice and humans have elevated skeletal accumulation of the NADPH oxidase 4 (NOX4) enzyme. Mechanistically, we found that the *NOX4* locus contains iron-response element-like (IRE-like) sequences that are normally bound (and repressed) by the iron regulatory protein 1 (IRP1) protein. Binding with iron induces dissociation of IRP1 from the IRE-like sequences and thereby activates *NOX4* transcription. Elevated NOX4 increases lipid peroxide accumulation and causes obvious dysregulation of mitochondrial morphology and function in osteoblasts. Excitingly, the osteoporotic bone loss which we initially observed in an excessive-iron accumulating mouse line (*Hepc1*$^{-/-}$) was blocked upon treatment with the ferroptosis-inhibitor ferrostatin-1 (Ferr-1) and with the iron chelator deferoxamine (DFO), suggesting a potential therapeutic strategy for preventing osteoporotic bone loss based on disruption of ferroptosis.

Introduction

Osteoporosis is a degenerative disease of bone tissue known to be promoted by several factors including age, sex, heredity, and lifestyle [1]. Excess iron accumulation has been identified as an independent risk factor for osteoporosis in both clinical and experimental studies [2-5], this nutrient element is essential for the proper function of almost most organisms. In bone tissue specifically, iron is known to be involved in the proliferation and differentiation of osteoblasts and osteoclasts [6-8]. While required for normal cellular function, excess iron accumulation can promote production of deleterious reactive oxygen species (ROS), leading to cytotoxic effects including cell damage and death, and is known to contribute to the pathogenesis of diseases such as cirrhosis, heart disease, Alzheimer's disease, and osteoporosis [4, 9-11].

A variety of disorders can cause iron metabolism abnormality, such as β-thalassemia and hemochromatosis [12, 13]. Beyond pathological iron metabolism disorders, the iron level of postmenopausal women tends to increase year by year, owing to decreased estrogen levels and reduced rates of iron excretion. Supporting that this elevation of iron levels contributes to bone metabolism disorders, the rate of bone loss is significantly faster in women with elevated iron levels compared to peers with low iron [3, 14]. However, the molecular mechanisms underlying these phenomena are not well understood.

Ferroptosis is a form of non-apoptotic programmed cell death driven by iron-dependent lipid peroxidation that has been associated with multiple metabolic disorders and disrupted homeostasis [15-17]. Ferroptosis is distinct from apoptosis and autophagy [17-19], and it is known that antioxidant enzymes including glutathione peroxidase 4 (GPX4) normally prevent ferroptosis in cells by adequately quenching any lipid peroxides before they can accumulate to a level that drives ferroptosis induction. When the

antioxidant capacity of cells is diminished, cells become increasingly susceptible to ferroptosis. Both cystine depletion and the overproduction of reactive oxygen species (ROS, especially lipid peroxides) are known to exacerbate ferroptosis. Several studies have demonstrated the utility of using GPX4 as a molecular marker of ferroptosis [18-20]. GPX4 uses reduced glutathione (GSH) as a substrate to scavenge ROS, and can exert powerful antioxidant effects. Disrupted mitochondria are also characteristic of ferroptosis, excess iron accumulation in mitochondria strongly promotes ROS production and peroxidation of fatty acids, leading to condensed mitochondrial membrane densities and smaller overall mitochondrial volume [21-23]. Diminished mitochondrial crista and the rupture of outer mitochondrial membranes are also evident in cells undergoing ferroptosis [23]. However, ferroptosis and its characteristics could be potently suppressed and reversed by liposphilic antioxidants such as ferrostatin-1 (Ferr-1) or iron chelators such as deferoxamine (DFO) [15, 24, 25].

Although many aspects of ferroptosis are not yet understood, the activities of some enzymes play an essential role in iron and oxidoreduction metabolism including NADPH oxidase 4 (NOX4). NOX4 contains catalytic subunits that transfers electrons from nicotinamide adenine dinucleotide phosphate (NADPH) to oxygen, thereby forming ROS [26]. NOX4 was identified a mitochondrial targeting sequence, and has been demonstrated as a significant ROS source for various types of cells [27]. Hyperglycemia/hyperoxia environment, and the nuclear factor kappa-B (NF-κB) pathway promote *NOX4* expression, whereas *NOX4* expression is negatively regulated by a variety of antioxidant factors [27-29]. For bone tissues specifically, studies have shown that both *Nox4* mRNA expression and ROS production were increased when bone marrow monocytes were stimulated by receptor activator of nuclear factor-κB Ligand (RANKL) for differentiation into osteoclasts. In *Nox4* knockout mice, RANKL failed to activate two known osteoclast differentiation transcription factors, nuclear factor of activated T cells (NFATC1) and activator protein 1, and the *Nox4* knockout mouse had aberrantly wide and thick trabecular bones and global increases in bone mass [30, 31]. NOX4 has been found not only in phagocytes, but also in somatic cells, and contributes to major sources of ROS in many types of cells [26-33]. It is highly notable that that *Nox4* knockout mice had superior cardiac function compared to WT controls upon induction of a classical murine disease model of heart failure [33].

In this study, we found that excess iron accumulation increases NOX4 accumulation and causes mitochondrial dysfunction in both human and murine osteoblasts. Iron promotes the dissociation of the IRP1 protein from IRE-like sequences at the *NOX4* promoter, thus activating *NOX4* transcription. Elevated NOX4 enzyme levels lead to increased ROS production and accumulation of intracellular lipid peroxides to drive ferroptosis in osteoblasts. After confirming that ferroptosis and increased NOX4 levels occur in hepcidin-knockout-induced osteoporotic mice and human osteoporosis patients, we found that administration of the ferroptosis-inhibitor Ferr-1 or the iron chelator DFO rescues the bone loss phenotype of the osteoporotic model mice. Therefore, targeting NOX4 and ferroptosis may represent a potential therapeutic avenue for treating iron-induced osteoporosis.

Results

Excess iron induced osteoblast cell death

To investigate the potential role of ferroptosis in osteoblast cells, we cultured hFOB1.19 human osteoblasts treated with iron dextran (Fe, 0, 200, 400, 600, 800, 1000 μg/mL) as well as the known ferroptosis inducer erastin as a positive control (0, 5, 10, 15, 20, 25 μM). Fe, like erastin, caused cell death in a dose-dependent manner in cultured hFOB1.19 cells (Fig. 1a and b). To determine whether Fe-induced cell death can be inhibited by ferroptosis-inhibitor ferrostatin-1 (Ferr-1), hFOB1.19 human osteoblasts were treated with different dosages of Ferr-1 prior to Fe exposure. Indeed, treatment with 5 μM Ferr-1 significantly protected cells against Fe-induced cell death (Fig. 1a and b). We next monitored glutathione peroxidase 4 (GPX4) level and found that the GPX4 protein was reduced in a dose-dependent manner upon exposure to Fe and to erastin (Fig. 1c and d). Further, Ferr-1 pre-treatment prevented the impact of Fe on the GPX4 level (Fig. 1c and d). Transmission electron microscopy (TEM) analysis revealed that the ferroptosis marker substantial morphological changes in mitochondria treated with iron, which exhibited shrinkage, dark staining, and a reduction in the number of mitochondrial ridges upon iron stimulation (Supplementary Fig. 1) [23]. To further investigate the impact of ferroptosis induced by excess iron on osteogenic differentiation and mineralization, ALP and alizarin red staining were performed and the results revealed that iron incubated osteoblasts exhibited an inhibited differentiation and mineralization compared to Ctrl group (Supplementary Fig. 2a and b). qRT-PCR for osteogenesis-related genes *ALP*, *RUNX2*, *OCN* revealed their downregulation existed in iron accumulated osteoblasts (Supplementary Fig. 2c-e). The fact that iron can induce hFOB1.19 human osteoblast cell death, and our finding that this cell death can be blocked by pretreatment with a known ferroptosis inhibitor together indicate that human osteoblasts are sensitive to iron-induced ferroptosis.

Excess iron induced bone-loss in mice by ferroptosis

We next conducted experiments using hepcidin knockout (*Hepc1*$^{-/-}$) mice—which decrease expression of hepcdin (Supplementary Fig. 3a and b) and accumulate iron (Supplementary Fig. 3c-e) in the liver and serum endogenously, and which are known to be susceptible to bone-loss—seeking to determine *in vivo* if ferroptosis contributes to excess-iron-induced bone loss [34]. We performed classic assays for detecting malondialdehyde (MDA) assays—an end-product formed during oxidation stress, and an indicator of ferroptosis—to assess lipid peroxides production and found that excess-iron-induced lipid peroxidation was blocked by inhibiting ferroptosis and by locally reducing the iron concentration [35]. Specifically, the typically elevated MDA level of *Hepc1*$^{-/-}$ mice (Fig. 2a) was significantly suppressed by administration of Ferr-1 (500 mg/kg) and of the iron chelation agent DFO (dose of 2.5μmol/kg twice a week from 20 to 28 weeks, Fig. 2a).

To further investigate the relationship(s) between bone loss and excess-iron-induced ferroptosis, we examined bone microstructure and the GPX4 level in femur bone by Micro-CT analysis together with immunofluorescence in *Hepc1*$^{-/-}$ mice. Confirming previous findings, the femur bone microstructure was deteriorated in *Hepc1*$^{-/-}$ mice compared to wild type (WT) mice, and the bone mineral density (BMD) was also obviously decreased (Fig. 2b and c). We also conducted immunofluorescence analysis of femurs

from sacrificed mice and found that the *Hepc1*$^{-/-}$ mice had a significantly reduced GPX4 levels at week 28 compared to WT controls (Fig. 2f and g). Treatment of *Hepc1*$^{-/-}$ mice with Ferr-1 from week 20 rescued both the reduced GPX4 phenotype (Fig. 2f and g) and the bone microstructure of the relevant parameters percent bone volume (BV/TV, Fig. 2d) and trabecular number (Tb.N, Fig. 2e) defect phenotypes at week 28. However, there was no change in trabecular thickness (Tb.Th, Supplementary Fig. 4a) and trabecular space (Tb.Sp, Supplementary Fig. 4b). Moreover, DFO treatment also rescued both of these phenotypes in *Hepc1*$^{-/-}$ mice (Fig. 2d-g). We also supplemented exogenous iron by giving ferric ammonium citrate (FAC) and treated mice with Ferr-1 and DFO from week 20, and observed the same trends as for the untreated *Hepc1*$^{-/-}$ mice (Supplementary Fig. 3, Fig. 2). Thus, our *in vivo* findings showing that Ferr-1 and DFO significantly increased BMD and the GPX4 level support that excess-iron-induced ferroptosis contributes to the reduced bone mass known for *Hepc1*$^{-/-}$ and FAC treated mice.

Ferroptosis is involved in excess iron associated osteoporosis

In light of these findings about excess-iron-induced ferroptotic cell death and bone loss in mice, and given that excess iron accumulation is a known independent risk factor for osteoporosis [2-5], we hypothesized that excess-iron-induced ferroptosis may contribute to the pathogenesis of osteoporosis. We pursued this idea by (1) collecting 11 samples from women who underwent hip replacement surgery (Fig. 3a), (2) determining the BMD of the contralateral hip by dual-energy X-ray absorptiometry and microarchitecture by Micro-CT, (3) detecting the concentration of serum ferritin, and (4) examining biomarkers of ferroptosis.

We found that 8/11 patients had elevated serum ferritin (a known one of the storage forms of iron) levels (Fer > 150 μg/L), and had significantly lower BMD at their collum femoris (Fig. 3b), findings consistent with previous prospective reports [2]. The bone microarchitecture of the high ferritin group was also abnormal compared to the normal ferritin group samples. The BMD (Fig. 3c and d), BV/TV (Fig. 3e) and Tb.N (Fig. 3f) were decreased whereas the Tb.Sp (Fig. 3g) was increased in the high ferritin group, there was no significant difference in Tb.Th (Fig. 3h). These results support an association between excess iron accumulation and low bone mass in female human hip-replacement patients.

We also assessed ferroptosis by measuring the levels of MDA and GPX4 and found that the high ferritin patients had significantly higher levels of MDA in undecalcified human trabecular bone biopsies (Fig. 3i). Immunofluorescence analysis showed that GPX4 levels were significantly lower in the bone samples of the high ferritin group (Fig. 3j and k). These biomarker changes again support an association of excess iron with susceptibility to ferroptosis in human bone.

Ferritin concentration is associated with decreased bone formation in women

These potential associations promoted us to assess how iron may contribute to bone-loss in a larger population cohort. We collected physical examination data for 214 women exhibiting BMD (supplemental Table 1), including the detected serum levels of ferritin, procollagen type 1 N propeptide (P1NP, a known

bone formation indicator), and C-terminal telopeptide of type 1 collagen (β-CTX, a known bone resorption indicator).

Multiple linear regression (MLR) was carried out to investigate potential relationships between serum ferritin, lumbar, and collum femoris BMD. We found a significant negative correlation between serum ferritin and BMD of the lumbar spine and femoral neck (simple correlation coefficients r= -0.17731, -0.16246, respectively) (Fig. 4a and b). After adjusting for baseline age, height, and other variables (Supplementary Table 1), this negative correlation persisted (the partial correlation coefficients r' = -0.19587, P = 0.0066, -0.16655, P = 0.0213, Fig. 4a and b).

There was no significantly correlation between the ferritin concentration and the β-CTX level (Fig. 4c), the level of P1NP was significantly negatively correlated with ferritin concentration after adjustment (Fig. 4d). These findings indicate that excess iron contributes to the pathogenesis of osteoporosis, apparently doing so in a manner involving bone formation but not bone resorption.

Ferr-1 prevents iron-induced lipid peroxides accumulation and NADPH depletion

Lipid peroxides accumulation is a hallmark of ferroptosis [15-17]. We thus used a fluorescence sensor (BODIPY 581/591 C11) to examine lipid peroxides in hFOB1.19 human osteoblasts treated with the aforementioned ferroptosis inducer erastin (15 μM) or Fe (800 μg/mL) and found that both significantly increased intracellular lipid peroxide levels (*i.e.*, oxidized BODIPY C11 signal, Fig. 5a and c). We also found that pre-treatment with the ferroptosis inhibitor Ferr-1 or the iron chelator DFO blocked these erastin and Fe induced increases in intracellular lipid peroxide levels (Fig. 5a and c). Given that lipid peroxides formation in ferroptotic cells is known to occur downstream of NADPH [26, 36], we also monitored NADPH levels in the human osteoblasts using the iNap1 sensor [37, 38]. Erastin and Fe administration significantly reduced the NADPH level, and this reduction phenotype was rescued upon pre-treatment of the osteoblasts with Ferr-1 and with DFO (Fig. 5b and d). Collectively, these findings support that elevated iron levels contribute to lipid ROS/NAPDH dependent ferroptosis in osteoblasts.

The NOX4 locus contains iron-response element-like sequences

Having shown that erastin and Fe treatments depleted NADPH and increased lipid peroxide levels in osteoblasts, and given that NADPH is a known electron donor for NADPH oxidases (NOXs) mediated production of superoxide from oxygen [26], we next examined the potential role(s) of the *NOX* family *NOX1–5* and two dual oxidase genes (*DOUX1–2*) in osteoblast ferroptosis [39]. Both *NOX4* and *DOUX1* were highly expressed in hFOB1.19 human osteoblasts (Fig. 6a), but only *NOX4* was sensitive to an elevated Fe concentration, suggesting some function for the *NOX4* gene in excess-iron-induced lipid peroxidation and ferroptosis. Interestingly, we found that the *NOX4* locus contains two ($5'C_1A_2G_3A_4G_5N_6$) sequence that are quite similar to known iron-response elements (type C1G5 IREs, $5'C_1A_2G_3T_4G_5N_6$) in ferritin (Fig. 6b) [40].

Iron homeostasis maintenance requires the coordination of multiple iron metabolism genes and the known genetic network for this coordination involves IRE-based regulation including repression by the IPR1 and IRP2 proteins [40. 41]. To examine whether the IRE-like sequences of the *NOX4* locus are responsive to iron stimulation in human osteoblasts, we cloned the putative *NOX4* promoter (containing IRE-like sequences) and IRE-Like mutant sequences (M1 and M2) to support comparative analyses into the pGL4.17 firefly luciferase reporter vector (Fig. 6b and c) [42]. Iron stimulation activated transcription from the IRE-like but not the M1 or M2 sequences (Fig. 6d). Consistent with the promoter assay showing activation of *NOX4* mRNA transcription, iron stimulation of osteoblasts also induced accumulation of the NOX4 protein, and can be inhibited by *NOX4* knockdown (Fig. 6e and f). We also performed Cleavage Under Targets and Tagmentation (CUT&Tag) analysis to assess regulatory protein binding at the *NOX4* promoter using antibodies against IRP1 and IRP2 and found that iron stimulation caused dissociation of the IRP1 protein from the IRE-like sequences of the *NOX4* promoter (Fig. 6g) [43], no iron-induced dissociation was observed for the IRP2 protein (Fig. 6g). Further, iron is able to derepress the inhibition induced by IRP1 (Fig. 6d). These results indicate that the IRE-like sequences of the *NOX4* promoter are normally occupied by the negative transcriptional regulator IRP1, and an elevation in the iron content in osteoblast cells can induce the dissociation—and therefore transcriptional activation—of the NADPH-consuming oxidase enzyme NOX4. Our discovery of this iron-sensitive genetic network therefore suggests plausible mechanisms to help explain our earlier observations including the reduced NADPH levels and increased intracellular lipid peroxide levels in osteoblasts with elevated iron content.

Inhibiting NOX4 expression prevents iron-induced lipid peroxides accumulation and mitochondria activity

Major sources of cellular ROS include dysregulated electron transport chain function in mitochondria and the catalytic activity of NOX enzymes [44]. After our identification of *NOX4* as an iron-response gene, we wonder whether decreased NOX4 levels may rescue excess-iron-induced ferroptosis. First, we measured respiration parameters (including oxygen consumption rate (OCR)) in hFOB1.19 human osteoblasts to characterize any alterations mitochondrial function in response to various iron-related treatments (Fig. 7a). Iron and erastin induced significant increases in both basal respiration (Fig. 7b) and maximum respiration (Fig. 7c). Accordingly, spare respiration capacity was elevated in the iron-stimulated and erastin-treated osteoblasts (Fig. 7d). Also, ATP production and proton leakage were significantly higher in the iron and erastin treated osteoblasts compared to untreated controls (Fig. 7e and f). As expected, there was no significant difference in the OCR between control and small interfering RNA (siRNA)-mediated *NOX4* knockdown osteoblasts (Fig. 7a-f). This elevation of OCR in iron-stimulated and erastin-treated osteoblasts may augment ROS production and thus lipid peroxides formation to promote ferroptosis.

We also examined the cell lipid peroxide content using the aforementioned BODIPY 581/591 C11 sensor and measured mitochondrial lipid peroxide content using the MitoPeDPP fluorescence sensor [45, 46]. The levels of lipid peroxides increased in cells (Fig. 7g and h) and in mitochondria upon iron stimulation (Fig. 7i and j). These increases were both blocked in *NOX4* knockdown osteoblasts (Fig. 7g-j). Furthermore, the ferroptosis changes of mitochondria were upon iron stimulation (Fig. 7k), these changes

were not evident upon iron stimulation of *NOX4* knockdown osteoblasts (Fig. 7k). These results establish that NOX4 contributes to the formation of lipid peroxides in iron-stimulated osteoblasts. Moreover, these results support that this NOX4-mediated lipid peroxide accumulation causes substantial mitochondrial dysfunction.

Excess iron accumulation induced NOX4 expression in human osteoporotic tissues

Seeking to extend these biochemical and cellular insights to our mouse model and clinical contexts, we examined potential changes the NOX4 protein levels in femurs from *Hepc1*$^{-/-}$ mice and in the aforementioned osteoporotic bone samples obtained from hip replacement patients. The NOX4 protein level was significantly higher *Hepc1*$^{-/-}$ femurs compared WT femurs from 28 week-old mice, no such elevation was observed in femurs from the Ferr-1 or DFO treated mice (Fig. 7l and m). For the human tissues, the NOX4 protein level was significantly higher in the high serum ferritin group than the normal ferritin group samples (Fig. 7l and m). These *in vivo* results suggest that excess iron is associated with increased NOX4 levels in both murine and human bones.

Discussion

In the present study, we discovered that ferroptosis occurs in osteoblasts and show how iron causes dissociation of IRP1 to drive transcription of *NOX4*. We also show how increased NOX4 results in increases in NADPH consumption, ROS production, lipid peroxide accumulation, and multiple forms of mitochondrial disruption. Knockdown of NOX4 decreased lipid peroxide levels and prevented ferroptosis in osteoblasts (Graphical abstract). NOX4 expression was increased in both human and mouse osteoporotic bones, and we show that bone loss in *Hepc1*$^{-/-}$ (excess iron) mice can be prevented through ferrostatin-1, the chemical inhibition of ferroptosis, and through deferoxamine, the chelation of iron.

Osteoporosis is a chronic degenerative bone metabolic disease with multiple underlying pathogenic mechanisms caused by various risk factors [1], and it is known that cell death mechanisms (including apoptosis and autophagy) in osteoblasts functionally impact skeletal development and maintenance, and these processes have been linked to the pathogenesis of osteoporosis [47, 48]. Estrogen deficiency or aging, the two major causes of osteoporosis, have been linked with apoptosis in osteoblasts [1, 47]. Apoptosis of osteoblasts is accompanied by changes in apoptosis markers, including increased levels of pro-apoptotic factors (*e.g.*, Bim and Bak) and decreased levels of the pro-survival factor BclXL, as well as by up-regulation of p53 protein expression [49]. The deletion of Bak and p53 in osteoblasts increases BMD in mice [50].

Previous work has demonstrated that bone morphogenetic proteins (BMPs) contribute to bone forming [51]. During osteoblast differentiation, BMP-2 induces autophagy-related gene 7 (ATG7) expression, causes accumulation of autophagosomes, and increases autophagy activity [52]. In addition, blocking the autophagy receptor neighbor of BRCA1 gene 1 (NBR1) in mouse also results in increased osteoblast differentiation and activity [53]. Moreover, activating transcription factor 4 (ATF4) was reported to

promote osteoblast survival through the transcription of several autophagy genes, including microtubule-associated protein 1 light chain 3 (MAP1LC3) and ATG5 [54].

Ferroptosis is a kind of programmed cell death resulting from the accumulation of lipid peroxides, it is distinct from both apoptosis and autophagy [17-19]. Our study supports that ferroptosis is involved in normal osteoblast, and, moreover, that ferroptosis contributes to the etiopathology of osteoporosis. Ferroptosis is closely related to ROS, and mitochondria and ROS-generating enzymes like NOX4 are known sources of ROS in bone tissue [55, 56]. Recent studies have demonstrated that both mitochondria and NOX4 are integrally involved in ferroptosis [57, 58]. ROS generation occurs in mitochondria when a single electron is transferred to molecular oxygen from a site along the electron transport chain (ETC) or from the mitochondrial tricarboxylic acid (TCA) cycle. Mitochondria transfer more than 90% of the electron to O_2 to generate O_2^- as the terminal electron acceptor [59]. The TCA cycle and ETC promote ferroptosis by serving as the major source for cellular lipid peroxide production [23, 57]. NOX4 generates ROS with NADPH as substrate, and a study suggested that activating NOX4 resulted in overproduction lipid peroxides and triggered ferroptosis in glioma cells [25, 58]. Therefore, deepening our understanding for the regulation of NOX4 may have implications for understanding ferroptosis.

The promoter of the human *NOX4* gene contains the γ-activated sequence (GAS elements) and the antioxidant response element (ARE). The Janus tyrosine kinase/signal transducers and activators of transcription (JAK/STAT) signaling pathway induces transcription of *NOX4* when activated STATs bind to the GAS, while the nuclear factor-erythroid 2-related factor 2 (Nrf2) protein promotes NOX4 via ARE [28, 60]. Our previous study found that iron elevated mesenchymal stem cell (MSC) NOX4 protein expression [61]. Further, high expression of NOX4 can promote the differentiation of MSCs into adipocytes rather than osteoblasts [62, 63]. Our these results showing that excess iron increased lipid peroxide levels while decreasing NADPH levels (an electron donor for NOX4) support the speculation that iron-induced ferroptosis in osteoblasts may require NOX4. Consistently, we found genomic DNA sequences highly similar to a known IRE at the ferritin locus present in the regulatory region of *NOX4*. Moreover, we show that iron enhances luciferase reporter expression from a plasmid containing the sequences for this element. Our CUT&Tag assay showed that the negative transcriptional regulator IRP1 exhibited higher affinity binding to these sequences compared to IRP2, and we demonstrate that elevating the iron content in osteoblast cells can induce IRP1 dissociation. Our results also suggest that not only IRP1 of drosophila enters the nucleus where it interacts with histones, and affects transcription of iron metabolism genes [64], but vertebrate IRP1 nuclear localization.

“Cross-talk” between ROS derived from NOX and mitochondria, termed “ROS-induced ROS release”, has been proposed as a mechanism for ROS amplification in distinct subcellular compartments [65, 66]. It is known that NOX4 promotes the production of mitochondrial ROS [67]. NOX4 is constitutively active even without classical cytosolic subunits and does not depend on cytosolic activator proteins or regulatory domains, but is activated by polymerase delta-interactive protein 2 (Poldip2), a mitochondrial protein known to regulate TCA cycle activity [60, 68]. Our results in the present study show that iron-induced accumulation of the NOX4 protein in osteoblasts increased the extent of mitochondrial dysregulation and

lipid peroxide accumulation. Further, NOX4 expression and the levels of MDA, an indicator of ferroptosis and cellular oxidative capacity, were increased in both human and mouse osteoporotic bone.

In conclusion, our discovery that excess iron accumulation associated osteoporosis and bone loss involves ferroptosis. It was exciting to note that we were able to block the osteoporotic bone loss observed in an excessive-iron accumulating mouse line (*Hepc1*$^{-/-}$) using the iron chelator DFO and the ferroptosis-inhibitor ferrostatin-1, which clearly suggests that the treatments presently under development for treating other ferroptosis related disorders might be applicable to treating bone loss disorders.

Methods And Materials

Cell culture and treatment

The hFOB1.19 and SaOS-2 osteoblast cell line were purchased from Procell Life Science & Technology. The cells were cultured according to the procedures of American Type Culture Collection (Manassas). hFOB1.19 cells were maintained in α-MEM (HyClone) supplemented with 10% foetal bovine serum (FBS, Biological Industries) and 0.3 g/L G418 (Sigma-Aldrich), whereas Saos-2 cells were maintained in McCoy5A medium (ATCC) supplemented with 15% of FBS. hFOB1.19 cells were cultured in a humidifed incubator with 5% CO2 at 33.4 °C and Saos-2 cells at 37 °C. The medium was replaced three times a week. Iron dextran (Fe, Sigma-Aldrich) was used to simulate an iron accumulation environment in vitro. Erastin (Sigma-Aldrich) was used as positive control for cell ferroptosis. Deferoxamine (DFO, Sigma-Aldrich) and Ferrostatin-1 (Ferr-1, Sigma-Aldrich) were used to inhibit Fe or erastin induced cell death. All samples were collected for relative assays.

Cell proliferation assay

hFOB1.19 osteoblast cells were seeded (10^3 cells per well) in 96-well plates. After cells were treated with erastin or Fe or/and Ferr-1 or/and DFO, a solution containing fresh medium (90 μl) and CCK-8 reactant (10 μl) (Dojindo) was added to each well, and cells were incubated at 37 °C for 1.5 h in the dark followed by addition of stop buffer. Absorbance at 450 nm was then measured using an enzyme-labelled instrument (Thermo). All operations were performed in accordance with the manufacturer's instructions.

Mice

The *Hepc1*$^{-/-}$ mice were used for endogenous iron accumulation mice model in this study [34]. The mice were housed in the specific pathogen free barrier system with normal diet in the animal facility of Soochow University. Genotype was verified by PCR of tail DNA samples. 20-week-old C57BL/6 wild-type mice were administered intraperitoneal injection of 0.1 g kg^{-1} $week^{-1}$ of ferric ammonium citrate (FAC, Sigma-Aldrich) for 8 weeks to establish exogenous iron accumulation model [5]. The mouse tissues were collected at 28 weeks old. All animal experiments were approved by the institutional animal care and use committee of Soochow University.

Measurement of hepcidin, ferritin and MDA content

The levels of mouse serum hepcidin and ferritinwere detected using the following ELISA kits: hepcidin (ElabScoemce) and Ferritin (abcam). Human bone and mouse serum malondialdehyde (MDA) content was measured using a kit (Beyotime). All the procedures were performed according to the manufacturers' instructions.

Human bone samples

Patients (11 individuals) admitted to our hospital with hip fractures were divided into two groups as Fer <150 and Fer >150 μg/L in terms of ferritin level. Whole blood samples for ferritin and other clinical indicators were collected from patients within 24 hours of admission. Areal bone mineral density (BMD) in collum femoris was measured by dual-energy X-ray absorptiometry (DXA). All patients were enrolled if the following criteria were met: pertrochanteric fracture and indication of a surgical treatment. Patients who suffered from inflammation, metabolic endocrine diseases, and malignancy and those who received medicines affecting bone metabolism were excluded. Human bone samples were collected from patients who were admitted to our hospital with hip fractures and required a surgical intervention. Bone samples were collected during proximal femoral nails (PFN) for intertrochanteric femur fractures using a special instrument that is 6 mm in diameter. Fresh samples obtained during PFN were divided into two halves for micro-CT scanning, immunofluorescence, MDA content detection, and western blot. Iatrogenic bone loss did not occur from the surgery itself. Informed consent was obtained from each patient before the procedure, and this process was approved by the institutional review board of the Second Affiliated Hospital of Soochow University.

Physical examination data

A total of 214 individuals physical examination results were analysis for blood test. The physical examination information is from Physical Examination Center, the Second Affiliated Hospital of Soochow University.

Micro-CT analysis

Mouse femora and fresh human bone samples obtained during surgery were fixed in 4% paraformaldehyde for 48 hours, then scanned and analyzed by micro-CT (SkyScan 1174). The acquisition settings were as follows: X-ray voltage = 50 kV, X-ray = 800 μA, filter = 0.5 mm aluminum, rotation step = 0.7°, and image pixel size = 10.3 μm. After scanning, images were reconstructed using NRecon software. Parameters were performed using CTAn software, and 3D image reconstruction were performed using CTvox software. For the human bone samples, the volume of interest (VOI) was outlined by a rectangular box-sized 1.5 mm × 2.0 mm × 1.5 mm, whereas for mouse bone samples, the VOI (100 slices) was outlined starting from a point ~ 0.7 mm proximal to the distal growth plate and extending 1.0 mm toward the diaphysis. The following parameters of the trabecular bone were calculated: bone mineral

density (BMD, g/cm^3), the relevant parameters percent bone volume (BV/TV, %), trabecular thickness (Tb.Th, mm), trabecular number (Tb.N, /mm), trabecular separation (Tb.Sp, mm).

Bone immunofluorescence analysis

The human and mouse bone samples used for micro-computed tomography scanning were decalcified in 0.5 M EDTA solution for 4 weeks with the change of solution twice a week. The tissues were then dehydrated using 20% sucrose and 2% polyvinylpyrrolidone solution for 2 week at 4 °C and then embedded in O.C.T. compound (Tissue-Tek). Cryosections (10 μm) were prepared using freezing microtome (Leica, Wetzlar) for immunostaining. The bone sections were washed three times with 0.3% PBST (Triton X-100) and blocked with 5% bovine serum albumin in PBS for 1 hour. Sections were incubated with primary antibody rabbit-anti-human (mouse) Glutathione Peroxidase 4 (GPX4, abcam) at 4 °C overnight. After three washes with 0.3% PBST, the sections were then incubated with fluorescein-conjugated secondary antibody together with nuclear counterstaining dye (DAPI) at room temperature in the dark. After another three washes, slides were mounted with 50% glycerol. The processed sections were visualized and imaged using a Multiphoton Laser Scanning Microscope (Olympus).

Western blot assays

Human and mouse bone samples were ground into powder with the liquid nitrogen and then lysed using RIPA solution containing protease inhibitor (Roche) on ice for 30 min. Cells were washed with PBS and then lysed using RIPA solution containing protease inhibitor on ice for 30 min. Bone and cell lysates centrifuged, and the supernatants were then collected. The collected supernatants were separated by SDS-polyacrylamide gel electrophoresis and blotted onto transfer membranes (Immobilon). Membranes were then incubated with the following specific antibodies: GPX4 (abcam), NADPH oxidase 4 (NOX4, abcam). The membranes were visualized with a solution of 100 mM Tris-HCl, luminal, 30% H_2O_2, and coumaric acid.

Lipid peroxides and NADPH assays

For lipid peroxides detection, cells were incubated in the dark at 37℃ in serum-free medium containing 2 μM BODIPY 581/591 C11 sensor (Invtrogene) for cellular lipid peroxides measure, and 0.5 μM MitoPeDPP fluorescence sensor (Dojindo) for mitochondrial lipid peroxide content measure, and 500 nM Mito Tracker Deep Red FM mitochondria fluorescence sensor (Invtrogene) for mitochondria measure for 20 min. The cells were washed three times in serum-free medium to remove extracellular sensor and then incubated with Hoechst 33342 (Beyotime) at room temperature in the dark. Cells were immediately examined using a Confocal Microscope (Olympus).

SaOS-2 cells were cultured and treated in 35mm glass bottom culture dish (Cellvis). For NADPH detection, cells transfected with iNap1 sensor (iNap1 sensor was encoded fluorescent indicators for NADPH which was responsive only to NADPH concentrations and not to the NADPH/NADP$^+$ ratio. iNap1 sensor used in this study was provided by profession Yi Yang) using Lipofectamine Max (Invitrogen) in Opti-MEM

medium (Gibco), and follow the manufacturer's protocol for transfection details. Replacement with fresh medium at 4 - 6 hours post transfection. After 24 - 36 hours, remove the medium, rinse the cells twice with 1 mL of PBS for imaging with Confocal Microscope (Olympus).

Mitochondria morphology analysis by transmission electron microscopy

SaOS-2 (hFOB1.19 used in Supplementary Fig. 1) cell pellets were fixed in 2.5% electron microscopy grade glutaraldehyde in 0.1 M sodium cacodylate buffer pH 7.4. Transmission electron microscopy was performed using standard procedures by Nanjing Medical University Analysis and Testing Center.

Real-time PCR analysis

Total RNA was prepared from cells and mixed in 1 ml TRIzol. RNA was reversed transcribed with the PrimeScript Reverse Transcriptase Kit according to the manufacturer's protocol (Takara). cDNA (2 μg) was used for real-time quantitative PCR using SYBR Premix Ex Taq (Takara). The sequences of RT-PCR primers are listed in Supplementary Table 2.

siRNA knockdown

hFOB1.19 cells were transiently transfected with NOX4 siRNA using GP-siRNA-mate Plus (Genepharma). The sequence of the NOX4 siRNA was as follows: siRNA NOX4 forward, 5'-CCUCAGCAUCUGUUCUUAATT-3' and reverse, 5'-UUAAGAACAGAUGCUGAGGTT-3' (GenePharma).

Whole-cell respiration analysis

Mitochondrial respiration was measured using the Seahorse XF24 Extracellular Flux Analyzer (Seahorse Bioscience) according to the manufacturer's instructions. hFOB1.19 cells were seeded onto an XF24 microplate at 5000 cells/well. The cellular Oxygen Consumption Rate (OCR) was monitored in unbuffered assay medium (Sigma) supplemented with (in mM) 2 GlutaMAX (Gibco), 2.5 sodium pyruvate, and 25 glucose (pH 7.4 at 37 °C), following the sequential addition of oligomycin (1 μM), carbonyl cyanide 4-(trifluoromethoxy) phenylhydrazone (FCCP, 500 nM), and rotenone (Rot, 1 μM) and antimycin A (AA, 1 μM) or in KHB buffer (in mM, 111.3 NaCl, 4.7 KCl, 2.0 $MgSO_4$, 1.2 Na_2HPO_4, 2.5 glucose, 0.5 L-Carnitine). For fatty acid supported respiration, the 2.5 mM sodium pyruvate and 25 mM glucose were replaced with 200 μM palmitate. Basal respiration was calculate by subtracting the OCR in the presence of Rot and AA from that in the non-presence of oligomycin. Maximal respiration was calculated by subtracting the OCR in the presence of Rot and AA from that in the presence of FCCP. Spare respiratory capacity was calculated by subtracting the OCR in the presence of FCCP from that in the non-presence of oligomycin. ATP production was calculated by subtracting the OCR in the non-presence of oligomycin from that in the presence of oligomycin. Proton leak was calculated by subtracting the OCR in the presence of oligomycin from that in the presence of Rot. and AA.

Reporter assay

2000 base pair (bp) in the sequence upstream regulatory region of NOX4 were PCRed from humangenomic DNA using the primers P-H-NOX4 forward: ccggtacctgagctcgctagcGAGATAGAGTCTTGCTCTGTCGCA, reverse: cagtaccggattgccaagcttGGAAGCCCGAAGGCCCGG and were cloned into pGL4.17 vector to form a new reporter plasmid NOX4-luc. The 2 mutation sites in the sequence upstream of NOX4 were designed as follows: from 5'-CAGAG-3' to 5'-GTCTC-3', respectively, and named as NOX4-M1-luc and NOX4-M2-luc. SaOS-2 cells were plated at 12-well plate and cultured with different treatments. Reporter plasmids were transfected using Lipofectamine Max (Invitrogen). The luciferase activity was measured using the luciferase activity assay kit (Promega).

Iron regulatory protein1 (IRP1) overexpression

Human IRP1 cDNA was subcloned into pcDNA3.1 between the KpnI (5') and NotI (3') sites. The pcDNA3.1 and pGL4.1 plasmid vectors were transfected into SaOS-2 cells and measured the luciferase activity.

Cleavage Under Targets and Tagmentation (CUT&Tag) assay

CUT&Tag assay was performed as described previously with modifications using CUT&Tag Kit [43]. hFOB1.19 cells were treated with or without Fe for 24 h, and then washed with warm PBS twice. Then, 105 cells were washed with 500 µl of wash buffer, and centrifuged at 600 g for 3 min at room temperature. Cell pellets were resuspended with 100 µl of wash buffer. Concanavalin A-coated magnetic beads were added and incubated at room temperature for 10 min with slow rotation. Bead-bound cells were resuspended in 50µl of cold antibody buffer. Then, 1 µg of primary antibody (mouse monoclonal anti-IRP1 antibody, mouse monoclonal anti-IRP2 antibody, Santa Cruz) or normal mouse IgG was added and incubated at room temperature for 2 h with slow rotation. The primary antibody was removed using a magnet stand. Secondary antibody 0.5 µl was diluted in 50 µl of Dig-wash buffer and cells were incubated at room temperature for 1 h. Cells were washed three times with Dig-wash buffer to remove unbound antibodies. The Hyperactive pG-Tn5 Transposase adapter complex (TTE mix) was diluted in 100µl of Dig-300 buffer. Cells were incubated with 0.04 µM TTE mix at room temperature for 1 h. Cells were washed three times with Dig-300 buffer to remove unbound TTE mix. Cells were then resuspended in 300µl of tagmentation buffer and incubated at 37 °C for 1 h. To terminate tagmentation, 10 µl of 0.5 M EDTA, 3 µl of 10% SDS and 2.5 µl of 20 mg/ml Proteinase K were added to 300 µl of sample and incubated at 50 °C for 1 h. DNA was purified using phenol-chloroform-isoamyl alcohol extraction and ethanol precipitation as well as RNase A treatment.

For library amplification, 24 µl of DNA was mixed with 1 µl of TruePrep Amplify Enzyme, 10 µl of 5× TruePrep Amplify Enzyme buffer and 5 µl of ddH2O, as well as 5 µl of P5 and P7 primers from TruePrep Index Kit V2 for Illumina (Vazyme). A total volume of 50 µl of sample was placed in a Thermocycler using the following program: 72 °C for 3 min, 98 °C for 30 s, 20 cycles of 98 °C for 15 s, 60 °C for 30 s and 72 °C for 30 s, 72 °C for 5 min and hold at 4 °C.

To purify the PCR products, 60 μl 1.2× volumes of VAHTS DNA Clean Beads (Vazyme) were added and incubated at room temperature for 5 min. Libraries were washed twice with 80% ethanol and eluted in 22μl of ddH2O. Library DNA concentration was calculated with a Qubit dsDNA HS Assay kit (Invitrogen) and a Qubit Fluorimeter. Library DNA (20 μg) was used for real-time quantitative PCR using SYBR Premix Ex Taq (Takara) with forward primer, 5'-TCGCCCCTAGACAAAGGGG-3' and reverse primer, 5'-TACCCAGAGCCGGGTTTTC-3'.

Statistical analyses

Data were presented as mean ± standard deviation (SD). Statistical analysis was carried out as described in each corresponding figure legend. For comparisons between two groups, we used two-tailed Student's t tests. For comparisons among multiple groups, we used one-way analysis of variance (ANOVA). P values of 0.05 or less were considered statistically significant. Graphical presentation and statistical analyses were performed using GraphPad Prism 8 (GraphPad Software, USA). All representative experiments were repeated at least three times.

Abbreviations

NOX4	NADPH oxidase 4
IRE	iron-response element
IRP1	protein 1
Ferr-1	ferrostatin-1
DFO	deferoxamine
ROS	reactive oxygen species
GPX4	glutathione peroxidase 4
GSH	glutathione
NADPH	nicotinamide adenine dinucleotide phosphate
NF-κB	nuclear factor kappa-B
RANKL	nuclear factor-κB Ligand
NFATC1	nuclear factor of activated T cells
Fe	iron dextran
TEM	transmission electron microscopy
Hepc1$^{-/-}$	hepcidin knockout
MDA	malondialdehyde
WT	wild type
BMD	bone mineral density
FAC	ferric ammonium citrate
P1NP	procollagen type 1 N propeptide
β-CTX	C-terminal telopeptide of type 1 collagen
MLR	multiple linear regression
DOUX	two dual oxidase
CUT&Tag	Cleavage Under Targets and Tagmentation
OCR	oxygen consumption rate
siRNA	small interfering RNA
BMP	bone morphogenetic protein
ATG	autophagy-related gene
NBR1	neighbor of BRCA1 gene 1

ATF4	activating transcription factor 4
MAP1LC3	microtubule-associated protein 1 light chain 3
ETC	electron transport chain
TCA	tricarboxylic acid
ARE	antioxidant response element
JAK/STAT	Janus tyrosine kinase/signal transducers and activators of transcription
Nrf2	nuclear factor-erythroid 2-related factor 2
MSC	mesenchymal stem cell
Poldip2	polymerase delta-interactive protein 2
PFN	proximal femoral nail
VOI	volume of interest
BV/TV	relevant parameters percent bone volume
Tb.Th	trabecular thickness
Tb.N	trabecular number
Tb.Sp	rabecular separation

Declarations

Ethics declarations

Conflict of interest

The authors declare no competing interests.

Ethical approval

The data utilized human tissue for this study was approved by the institutional review board of the Second Affiliated Hospital of Soochow University (Ethics approval number: JD-LK-2020-028-01). All animal handling was approved by the institutional animal care and use committee of Soochow University (Ethics approval number: ECSU-201800093).

Consent to participate

This study does not involve human subjects.

Consent to publication

The study does not involve human participants and no consent for publication of images is required.

Availability of data and material

All data generated or analysed during this study are included in this published article and its supplementary information files. Further information is available from the corresponding author on reasonable request.

Acknowledgments

The authors would like to thank professor Yi Yang (East China University of Science and Technology, China) for generously providing the iNap1 sensor, and thank professor Dengshun Miao (Nanjing Medical University, China) for generously providing the technology of transmission electron microscopy, and thank Chao Li and Baoshi Yuan helped with experiment method guidance.

Funding

This study was supported by grants from the Natural Science Foundation of China (82072474), the National Natural Science Foundation of China for Youth (81803242), Clinical Madicine Technology Project of Jiangsu Province (BE2019661), Minsheng Science and Technology Project of Suzhou City (SS201814), health leading talents of Gusu City (GSWS2019004).

Author information

Hui Zhang, Aifei Wang and Guangfei Li contributed equally to this work.

Authors and Affiliations

Authors and Affiliations

Department of Orthopaedics, the Second Affiliated Hospital of Soochow University, Suzhou, 215004, China

Hui Zhang, Aifei Wang, Guangfei Li, Xiao Wang, Zihou Cao, Bin Chen, Keyu Zhu, Youjia Xu

Department of Orthopaedics, the First Affiliated Hospital of USTC, Division of Life Sciences and Medicine, University of Science and Technology of China, Hefei, Anhui, 230001, China

Hui Zhang

Jiangsu Key Laboratory of Neuropsychiatric Diseases and Cambridge-Su Genomic Resource Center, Medical School of Soochow University, Suzhou, Jiangsu, 215123, China

Qiaocheng Zhai, Zhengyun Huang, Ying Xu

Osteoporosis Clinical Center, the Second Affiliated Hospital of Soochow University, Suzhou, 215004, China

Hui Zhang, Aifei Wang, Guangfei Li, Xiao Wang, Bin Chen, Keyu Zhu, Youjia Xu

Institute of Osteoporosis Diagnosis and Treatments of Soochow University, Suzhou 215004, China

Aifei Wang, Zihou Cao, Lulin Liu, Keyu Zhu, Youjia Xu

Department of Orthopaedics, Suzhou TCM Hospital Affiliated to Nanjing University of Chinese Medicine, Suzhou, 215004, China

Gongwen Liu

Contributions

HZ, Ying Xu and Youjia Xu designed the study. HZ, AW and G.Li performed most of the experiments. QZ and ZH plasmid construction. XW performed cell culture and RT-PCR experiments. ZC and LL helped with genotyping and mouse samples collection. G.Liu and BC performed Mirco-CT and helped with analyzing the data. KZ helped with human bone samples collection. HZ and Ying Xu wrote the manuscript. HZ, AW, G.Li, Ying Xu and Youjia Xu reviewed and revised the manuscript. Ying Xu and Youjia Xu approved the final version. All authors read, commented on and approved the final manuscript.

Corresponding authors

Correspondence to Ying Xu or Youjia Xu.

References

1. Hendrickx G, Boudin E, Van Hul W (2015) A look behind the scenes: the risk and pathogenesis of primary osteoporosis. Nat Rev Rheumatol 11:462-474
2. Kim BJ, Ahn SH, Bae SJ, Kim EH, Lee SH, Kim HK, Choe JW, Koh JM, Kim GS (2012) Iron overload accelerates bone loss in healthy postmenopausal women and middle-aged men: a 3-year retrospective longitudinal study. J Bone Miner Res 27:2279-2290
3. Liu G, Men P, Kenner GH, Miller SC (2006) Age-associated iron accumulation in bone: implications for postmenopausal osteoporosis and a new target for prevention and treatment by chelation. Biometals 19:245-251
4. Wang X, Chen B, Sun J, Jiang Y, Zhang H, Zhang P, Fei B, Xu Y (2018) Iron-induced oxidative stress stimulates osteoclast differentiation via NF-κB signaling pathway in mouse model. Metabolism 83:167-176
5. Tsay J, Yang Z, Ross FP, Cunningham-Rundles S, Lin H, Coleman R, Mayer-Kuckuk P, Doty SB, Grady RW, Giardina PJ, Boskey AL, Vogiatzi MG (2010) Bone loss caused by iron overload in a murine

model: importance of oxidative stress. Blood 116:2582-2589

6. Rautiainen S, Manson JE, Lichtenstein AH, Sesso HD (2016) Dietary supplements and disease prevention - a global overview. Nat Rev Endocrinol 12:407-420
7. Ishii KA, Fumoto T, Iwai K, Takeshita S, Ito M, Shimohata N, Aburatani H, Taketani S, Lelliott CJ, Vidal-Puig A, Ikeda K (2009) Coordination of PGC-1beta and iron uptake in mitochondrial biogenesis and osteoclast activation. Nat Med 15:259-266
8. Baschant U, Rauner M, Balaian E, Weidner H, Roetto A, Platzbecker U, Hofbauer LC (2016) Wnt5a is a key target for the pro-osteogenic effects of iron chelation on osteoblast progenitors. Haematologica 101:1499-1507
9. Shendge AK, Basu T, Panja S, Chaudhuri D, Mandal N (2018) An ellagic acid isolated from Clerodendrum viscosum leaves ameliorates iron-overload induced hepatotoxicity in Swiss albino mice through inhibition of oxidative stress and the apoptotic pathway. Biomed Pharmacother 106:454-465
10. Fang X, Wang H, Han D, Xie E, Yang X, Wei J, Gu S, Gao F, Zhu N, Yin X, Cheng Q, Zhang P, Dai W, Chen J, Yang F, Yang HT, Linkermann A, Gu W, Min J, Wang F (2019) Ferroptosis as a target for protection against cardiomyopathy. Proc Natl Acad Sci U S A 116:2672-2680
11. Liu Y, Nguyen M, Robert A, Meunier B (2019) Metal Ions in Alzheimer's Disease: A Key Role or Not. Acc Chem Res 52:2026-2035
12. Cappellini MD, Viprakasit V, Taher AT, Georgiev P, Kuo K, Coates T, Voskaridou E, Liew HK, Pazgal-Kobrowski I, Forni GL, Perrotta S, Khelif A, Lal A, Kattamis A, Vlachaki E, Origa R, Aydinok Y, Bejaoui M, Ho PJ, Chew LP, Bee PC, Lim SM, Lu MY, Tantiworawit A, Ganeva P, Gercheva L, Shah F, Neufeld EJ, Thompson A, Laadem A, Shetty JK, Zou J, Zhang J, Miteva D, Zinger T, Linde PG, Sherman ML, Hermine O, Porter J, Piga A (2020) A Phase 3 Trial of Luspatercept in Patients with Transfusion-Dependent β-Thalassemia. N Engl J Med 382:1219-1231
13. Demetz E, Tymoszuk P, Hilbe R, Volani C, Haschka D, Heim C, Auer K, Lener D, Zeiger LB, Pfeifhofer-Obermair C, Boehm A, Obermair GJ, Ablinger C, Coassin S, Lamina C, Kager J, Petzer V, Asshoff M, Schroll A, Nairz M, Dichtl S, Seifert M, von Raffay L, Fischer C, Barros-Pinkelnig M, Brigo N, Valente de Souza L, Sopper S, Hirsch J, Graber M, Gollmann-Tepeköylü C, Holfeld J, Halper J, Macheiner S, Gostner J, Vogel GF, Pechlaner R, Moser P, Imboden M, Marques-Vidal P, Probst-Hensch NM, Meiselbach H, Strauch K, Peters A, Paulweber B, Willeit J, Kiechl S, Kronenberg F, Theurl I, Tancevski I, Weiss G (2020) The haemochromatosis gene Hfe and Kupffer cells control LDL cholesterol homeostasis and impact on atherosclerosis development. Eur Heart J
14. Huang X, Xu Y, Partridge NC (2013) Dancing with sex hormones, could iron contribute to the gender difference in osteoporosis. Bone 55:458-460
15. Dixon SJ, Lemberg KM, Lamprecht MR, Skouta R, Zaitsev EM, Gleason CE, Patel DN, Bauer AJ, Cantley AM, Yang WS, Morrison B, Stockwell BR (2012) Ferroptosis: an iron-dependent form of nonapoptotic cell death. Cell 149:1060-1072

16. Zhang Y, Shi J, Liu X, Feng L, Gong Z, Koppula P, Sirohi K, Li X, Wei Y, Lee H, Zhuang L, Chen G, Xiao ZD, Hung MC, Chen J, Huang P, Li W, Gan B (2018) BAP1 links metabolic regulation of ferroptosis to tumour suppression. Nat Cell Biol 20:1181-1192
17. Galluzzi L, Bravo-San Pedro JM, Vitale I, Aaronson SA, Abrams JM, Adam D, Alnemri ES, Altucci L, Andrews D, Annicchiarico-Petruzzelli M, Baehrecke EH, Bazan NG, Bertrand MJ, Bianchi K, Blagosklonny MV, Blomgren K, Borner C, Bredesen DE, Brenner C, Campanella M, Candi E, Cecconi F, Chan FK, Chandel NS, Cheng EH, Chipuk JE, Cidlowski JA, Ciechanover A, Dawson TM, Dawson VL, De Laurenzi V, De Maria R, Debatin KM, Di Daniele N, Dixit VM, Dynlacht BD, El-Deiry WS, Fimia GM, Flavell RA, Fulda S, Garrido C, Gougeon ML, Green DR, Gronemeyer H, Hajnoczky G, Hardwick JM, Hengartner MO, Ichijo H, Joseph B, Jost PJ, Kaufmann T, Kepp O, Klionsky DJ, Knight RA, Kumar S, Lemasters JJ, Levine B, Linkermann A, Lipton SA, Lockshin RA, López-Otín C, Lugli E, Madeo F, Malorni W, Marine JC, Martin SJ, Martinou JC, Medema JP, Meier P, Melino S, Mizushima N, Moll U, Muñoz-Pinedo C, Nuñez G, Oberst A, Panaretakis T, Penninger JM, Peter ME, Piacentini M, Pinton P, Prehn JH, Puthalakath H, Rabinovich GA, Ravichandran KS, Rizzuto R, Rodrigues CM, Rubinsztein DC, Rudel T, Shi Y, Simon HU, Stockwell BR, Szabadkai G, Tait SW, Tang HL, Tavernarakis N, Tsujimoto Y, Vanden Berghe T, Vandenabeele P, Villunger A, Wagner EF, Walczak H, White E, Wood WG, Yuan J, Zakeri Z, Zhivotovsky B, Melino G, Kroemer G (2015) Essential versus accessory aspects of cell death: recommendations of the NCCD 2015. Cell Death Differ 22:58-73
18. Friedmann Angeli JP, Schneider M, Proneth B, Tyurina YY, Tyurin VA, Hammond VJ, Herbach N, Aichler M, Walch A, Eggenhofer E, Basavarajappa D, Rådmark O, Kobayashi S, Seibt T, Beck H, Neff F, Esposito I, Wanke R, Förster H, Yefremova O, Heinrichmeyer M, Bornkamm GW, Geissler EK, Thomas SB, Stockwell BR, O'Donnell VB, Kagan VE, Schick JA, Conrad M (2014) Inactivation of the ferroptosis regulator Gpx4 triggers acute renal failure in mice. Nat Cell Biol 16:1180-1191
19. Yang WS, SriRamaratnam R, Welsch ME, Shimada K, Skouta R, Viswanathan VS, Cheah JH, Clemons PA, Shamji AF, Clish CB, Brown LM, Girotti AW, Cornish VW, Schreiber SL, Stockwell BR (2014) Regulation of ferroptotic cancer cell death by GPX4. Cell 156:317-331
20. Viswanathan VS, Ryan MJ, Dhruv HD, Gill S, Eichhoff OM, Seashore-Ludlow B, Kaffenberger SD, Eaton JK, Shimada K, Aguirre AJ, Viswanathan SR, Chattopadhyay S, Tamayo P, Yang WS, Rees MG, Chen S, Boskovic ZV, Javaid S, Huang C, Wu X, Tseng YY, Roider EM, Gao D, Cleary JM, Wolpin BM, Mesirov JP, Haber DA, Engelman JA, Boehm JS, Kotz JD, Hon CS, Chen Y, Hahn WC, Levesque MP, Doench JG, Berens ME, Shamji AF, Clemons PA, Stockwell BR, Schreiber SL (2017) Dependency of a therapy-resistant state of cancer cells on a lipid peroxidase pathway. Nature 547:453-457
21. Du J, Zhou Y, Li Y, Xia J, Chen Y, Chen S, Wang X, Sun W, Wang T, Ren X, Wang X, An Y, Lu K, Hu W, Huang S, Li J, Tong X, Wang Y (2020) Identification of Frataxin as a regulator of ferroptosis. Redox Biol 32:101483
22. Duncan OF, Granat L, Ranganathan R, Singh VK, Mazaud D, Fanto M, Chambers D, Ballard CG, Bateman JM (2018) Ras-ERK-ETS inhibition alleviates neuronal mitochondrial dysfunction by reprogramming mitochondrial retrograde signaling. PLoS Genet 14:e1007567

23. Wang H, Liu C, Zhao Y, Gao G (2020) Mitochondria regulation in ferroptosis. Eur J Cell Biol 99:151058
24. Gao M, Monian P, Pan Q, Zhang W, Xiang J, Jiang X (2016) Ferroptosis is an autophagic cell death process. Cell Res 26:1021-1032
25. Belavgeni A, Bornstein SR, von Mässenhausen A, Tonnus W, Stumpf J, Meyer C, Othmar E, Latk M, Kanczkowski W, Kroiss M, Hantel C, Hugo C, Fassnacht M, Ziegler CG, Schally AV, Krone NP, Linkermann A (2019) Exquisite sensitivity of adrenocortical carcinomas to induction of ferroptosis. Proc Natl Acad Sci U S A 116:22269-22274
26. Geiszt M, Kopp JB, Várnai P, Leto TL (2000) Identification of renox, an NAD(P)H oxidase in kidney. Proc Natl Acad Sci U S A 97:8010-8014
27. Gorin Y, Block K (2013) Nox4 and diabetic nephropathy: with a friend like this, who needs enemies. Free Radic Biol Med 61:130-142
28. Manea A, Tanase LI, Raicu M, Simionescu M (2010) Jak/STAT signaling pathway regulates nox1 and nox4-based NADPH oxidase in human aortic smooth muscle cells. Arterioscler Thromb Vasc Biol 30:105-112
29. Pendyala S, Moitra J, Kalari S, Kleeberger SR, Zhao Y, Reddy SP, Garcia JG, Natarajan V (2011) Nrf2 regulates hyperoxia-induced Nox4 expression in human lung endothelium: identification of functional antioxidant response elements on the Nox4 promoter. Free Radic Biol Med 50:1749-1759
30. Werner SL, Sharma R, Woodruff K, Horn D, Harris SE, Gorin Y, Lee DY, Hua R, Gu S, Fajardo RJ, Habib SL, Jiang JX (2020) CSF-1 in Osteocytes Inhibits Nox4-mediated Oxidative Stress and Promotes Normal Bone Homeostasis. JBMR Plus 4:e10080
31. Goettsch C, Babelova A, Trummer O, Erben RG, Rauner M, Rammelt S, Weissmann N, Weinberger V, Benkhoff S, Kampschulte M, Obermayer-Pietsch B, Hofbauer LC, Brandes RP, Schröder K (2013) NADPH oxidase 4 limits bone mass by promoting osteoclastogenesis. J Clin Invest 123:4731-4738
32. Tian Q, Wu S, Dai Z, Yang J, Zheng J, Zheng Q, Liu Y (2016) Iron overload induced death of osteoblasts in vitro: involvement of the mitochondrial apoptotic pathway. PeerJ 4:e2611
33. Kuroda J, Ago T, Matsushima S, Zhai P, Schneider MD, Sadoshima J (2010) NADPH oxidase 4 (Nox4) is a major source of oxidative stress in the failing heart. Proc Natl Acad Sci U S A 107:15565-15570
34. Shen GS, Yang Q, Jian JL, Zhao GY, Liu LL, Wang X, Zhang W, Huang X, Xu YJ (2014) Hepcidin1 knockout mice display defects in bone microarchitecture and changes of bone formation markers. Calcif Tissue Int 94:632-639
35. Wang H, An P, Xie E, Wu Q, Fang X, Gao H, Zhang Z, Li Y, Wang X, Zhang J, Li G, Yang L, Liu W, Min J, Wang F (2017) Characterization of ferroptosis in murine models of hemochromatosis. Hepatology 66:449-465
36. Brewer TF, Garcia FJ, Onak CS, Carroll KS, Chang CJ (2015) Chemical approaches to discovery and study of sources and targets of hydrogen peroxide redox signaling through NADPH oxidase proteins. Annu Rev Biochem 84:765-790

37. Tao R, Zhao Y, Chu H, Wang A, Zhu J, Chen X, Zou Y, Shi M, Liu R, Su N, Du J, Zhou HM, Zhu L, Qian X, Liu H, Loscalzo J, Yang Y (2017) Genetically encoded fluorescent sensors reveal dynamic regulation of NADPH metabolism. Nat Methods 14:720-728
38. Zou Y, Wang A, Shi M, Chen X, Liu R, Li T, Zhang C, Zhang Z, Zhu L, Ju Z, Loscalzo J, Yang Y, Zhao Y (2018) Analysis of redox landscapes and dynamics in living cells and in vivo using genetically encoded fluorescent sensors. Nat Protoc 13:2362-2386
39. Montezano AC, Touyz RM (2014) Reactive oxygen species, vascular Noxs, and hypertension: focus on translational and clinical research. Antioxid Redox Signal 20:164-182
40. Rogers JT, Xia N, Wong A, Bakshi R, Cahill CM (2019) Targeting the Iron-Response Elements of the mRNAs for the Alzheimer's Amyloid Precursor Protein and Ferritin to Treat Acute Lead and Manganese Neurotoxicity. Int J Mol Sci 20
41. Hernández-Gallardo AK, Missirlis F (2020) Cellular iron sensing and regulation: Nuclear IRP1 extends a classic paradigm. Biochim Biophys Acta Mol Cell Res 1867:118705
42. Thomson AM, Rogers JT, Leedman PJ (1999) Iron-regulatory proteins, iron-responsive elements and ferritin mRNA translation. Int J Biochem Cell Biol 31:1139-1152
43. Lu D, Liu L, Sun Y, Song J, Yin Q, Zhang G, Qi F, Hu Z, Yang Z, Zhou Z, Hu Y, Zhang L, Ji J, Zhao X, Jin Y, McNutt MA, Yin Y (2020) The phosphatase PAC1 acts as a T cell suppressor and attenuates host antitumor immunity. Nat Immunol 21:287-297
44. Habtetsion T, Ding ZC, Pi W, Li T, Lu C, Chen T, Xi C, Spartz H, Liu K, Hao Z, Mivechi N, Huo Y, Blazar BR, Munn DH, Zhou G (2018) Alteration of Tumor Metabolism by CD4+ T Cells Leads to TNF-α-Dependent Intensification of Oxidative Stress and Tumor Cell Death. Cell Metab 28:228-242.e6
45. Martinez AM, Kim A, Yang WS (2020) Detection of Ferroptosis by BODIPY™ 581/591 C11. Methods Mol Biol 2108:125-130
46. Álvarez-Córdoba M, Fernández Khoury A, Villanueva-Paz M, Gómez-Navarro C, Villalón-García I, Suárez-Rivero JM, Povea-Cabello S, de la Mata M, Cotán D, Talaverón-Rey M, Pérez-Pulido AJ, Salas JJ, Pérez-Villegas EM, Díaz-Quintana A, Armengol JA, Sánchez-Alcázar JA (2019) Pantothenate Rescues Iron Accumulation in Pantothenate Kinase-Associated Neurodegeneration Depending on the Type of Mutation. Mol Neurobiol 56:3638-3656
47. Komori T (2016) Cell Death in Chondrocytes, Osteoblasts, and Osteocytes. Int J Mol Sci 17
48. Wang S, Deng Z, Ma Y, Jin J, Qi F, Li S, Liu C, Lyu FJ, Zheng Q (2020) The Role of Autophagy and Mitophagy in Bone Metabolic Disorders. Int J Biol Sci 16:2675-2691
49. Komori T (2016) Glucocorticoid Signaling and Bone Biology. Horm Metab Res 48:755-763
50. Jilka RL, O'Brien CA, Roberson PK, Bonewald LF, Weinstein RS, Manolagas SC (2014) Dysapoptosis of osteoblasts and osteocytes increases cancellous bone formation but exaggerates cortical porosity with age. J Bone Miner Res 29:103-117
51. Zhang X, Yu Q, Wang YA, Zhao J (2018) Dose reduction of bone morphogenetic protein-2 for bone regeneration using a delivery system based on lyophilization with trehalose. Int J Nanomedicine 13:403-414

52. Ozeki N, Mogi M, Hase N, Hiyama T, Yamaguchi H, Kawai R, Matsumoto T, Nakata K (2016) Bone morphogenetic protein-induced cell differentiation involves Atg7 and Wnt16 sequentially in human stem cell-derived osteoblastic cells. Exp Cell Res 347:24-41
53. Whitehouse CA, Waters S, Marchbank K, Horner A, McGowan NW, Jovanovic JV, Xavier GM, Kashima TG, Cobourne MT, Richards GO, Sharpe PT, Skerry TM, Grigoriadis AE, Solomon E (2010) Neighbor of Brca1 gene (Nbr1) functions as a negative regulator of postnatal osteoblastic bone formation and p38 MAPK activity. Proc Natl Acad Sci U S A 107:12913-12918
54. Yang X, Karsenty G (2004) ATF4, the osteoblast accumulation of which is determined post-translationally, can induce osteoblast-specific gene expression in non-osteoblastic cells. J Biol Chem 279:47109-47114
55. Zheng CX, Sui BD, Qiu XY, Hu CH, Jin Y (2020) Mitochondrial Regulation of Stem Cells in Bone Homeostasis. Trends Mol Med 26:89-104
56. Atashi F, Modarressi A, Pepper MS (2015) The role of reactive oxygen species in mesenchymal stem cell adipogenic and osteogenic differentiation: a review. Stem Cells Dev 24:1150-1163
57. Gao M, Yi J, Zhu J, Minikes AM, Monian P, Thompson CB, Jiang X (2019) Role of Mitochondria in Ferroptosis. Mol Cell 73:354-363.e3
58. Wang Z, Ding Y, Wang X, Lu S, Wang C, He C, Wang L, Piao M, Chi G, Luo Y, Ge P (2018) Pseudolaric acid B triggers ferroptosis in glioma cells via activation of Nox4 and inhibition of xCT. Cancer Lett 428:21-33
59. Go YM, Jones DP (2008) Redox compartmentalization in eukaryotic cells. Biochim Biophys Acta 1780:1273-1290
60. Wang H, Liu C, Zhao Y, Gao G (2020) Mitochondria regulation in ferroptosis. Eur J Cell Biol 99:151058
61. Yuan Y, Xu F, Cao Y, Xu L, Yu C, Yang F, Zhang P, Wang L, Shen G, Wang J, Xu Y (2019) Iron Accumulation Leads to Bone Loss by Inducing Mesenchymal Stem Cell Apoptosis Through the Activation of Caspase3. Biol Trace Elem Res 187:434-441
62. Kanda Y, Hinata T, Kang SW, Watanabe Y (2011) Reactive oxygen species mediate adipocyte differentiation in mesenchymal stem cells. Life Sci 89:250-258
63. Schröder K, Wandzioch K, Helmcke I, Brandes RP (2009) Nox4 acts as a switch between differentiation and proliferation in preadipocytes. Arterioscler Thromb Vasc Biol 29:239-245
64. Huynh N, Ou Q, Cox P, Lill R, King-Jones K (2019) Glycogen branching enzyme controls cellular iron homeostasis via Iron Regulatory Protein 1 and mitoNEET. Nat Commun 10:5463
65. Dikalov S (2011) Cross talk between mitochondria and NADPH oxidases. Free Radic Biol Med 51:1289-1301
66. Fukai T, Ushio-Fukai M (2020) Cross-Talk between NADPH Oxidase and Mitochondria: Role in ROS Signaling and Angiogenesis. Cells 9

67. Kim YM, Kim SJ, Tatsunami R, Yamamura H, Fukai T, Ushio-Fukai M (2017) ROS-induced ROS release orchestrated by Nox4, Nox2, and mitochondria in VEGF signaling and angiogenesis. Am J Physiol Cell Physiol 312:C749-749C764
68. Paredes F, Sheldon K, Lassègue B, Williams HC, Faidley EA, Benavides GA, Torres G, Sanhueza-Olivares F, Yeligar SM, Griendling KK, Darley-Usmar V, San Martin A (2018) Poldip2 is an oxygen-sensitive protein that controls PDH and αKGDH lipoylation and activation to support metabolic adaptation in hypoxia and cancer. Proc Natl Acad Sci U S A 115:1789-1794

Figures

Figure 1

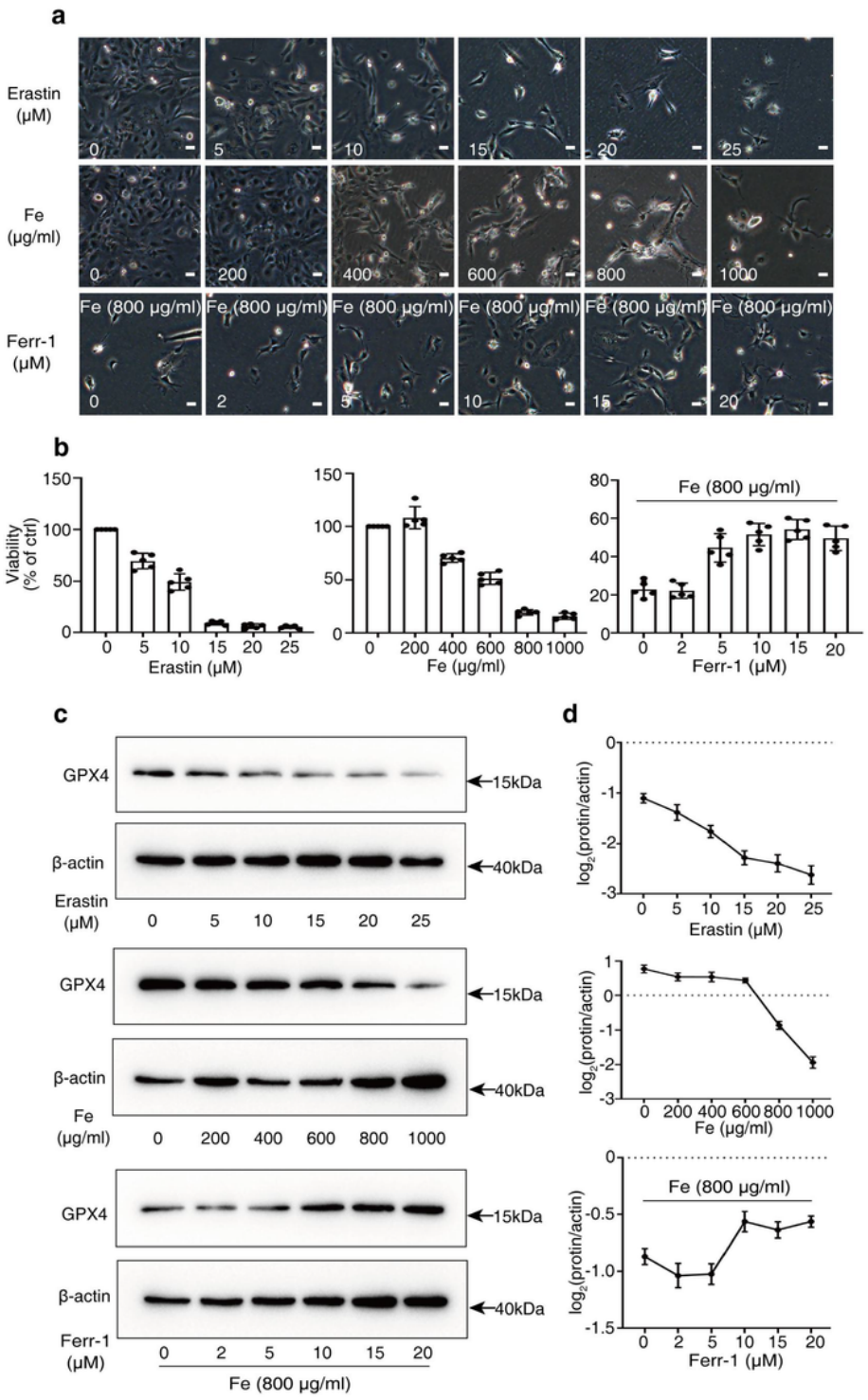

Figure 1

Excess iron induced osteoblast cell ferroptosis. (a) Visualization of hFOB1.19 human osteoblast cell viability upon exposure to different concentrations of ferroptosis inducers erastin (0, 5, 10, 15, 20, 25 μM) or iron dextran (Fe, 0, 200, 400, 600, 800, 1000 μg/mL) or to the ferroptosis inhibitor ferrostatin-1 (Ferr-1, 0, 2, 5, 10, 15, 20 μM). Scale bar, 50 μm. **(b)** Cell viability measured with CCK-8 assays (n = 5 biologically independent cell samples). **(c)** Immunoblotting of GPX4 protein levels in hFOB1.19 cells treated with

erastin, Fe, or Ferr-1. **(d)** Quantitation of the GPX4 band intensity from (**c**), protein levels were normalized to β-actin.

Figure 2

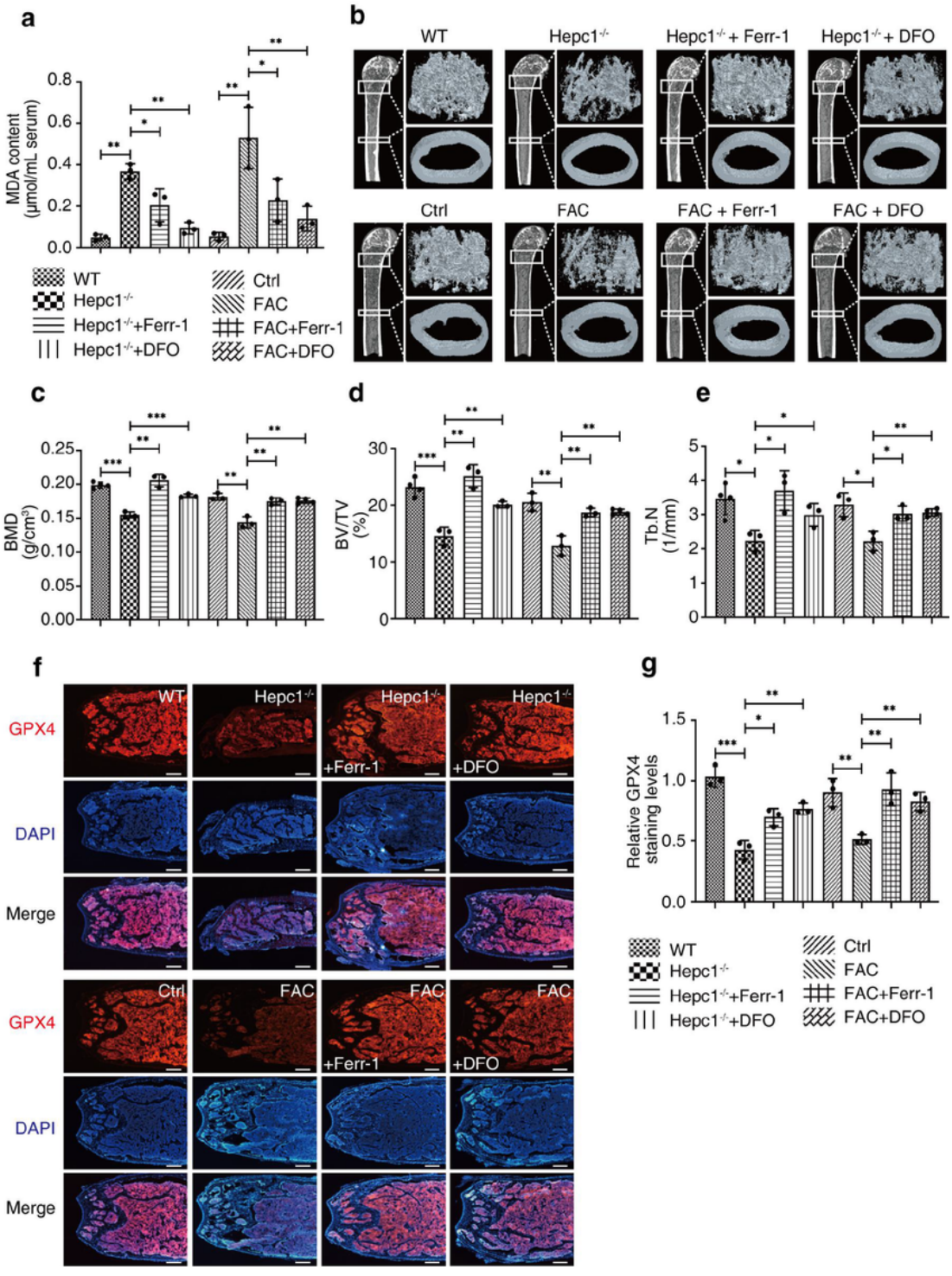

Figure 2

Excess iron accumulation induces bone loss in mice. (a) Malondialdehyde (MDA) content was measured in the serum of mice (n = 3 biologically independent mouse samples). Micro-CT to evaluate mice bone

mineral density (BMD) and bone microarchitecture. **(b)** Representative Micro-CT reconstructed three-dimensional images of mouse trabecular bone of 28-week-old mice (n = 3 or 4, biologically independent mouse samples). **(c-e)** Micro-CT quantification of the trabecular bone index of mouse bone samples. The parameters examined included (**c**) BMD, (**d**) percent bone volume (BV/TV), and (**e**) trabecular number (Tb.N). **(f)** Immunofluorescence of decalcified bone tissue (frozen sections) stained with an antibody against glutathione peroxidase 4 (GPX4) (red) and DAPI (blue). Scale bar, 500 μm. **(g)** Quantification of GPX4 staining levels in the mouse trabecular bone (from **f**, n = 3 biologically independent mouse samples). Assessed samples included mice treated with normal saline (WT, Ctrl, *Hepc1*$^{-/-}$) or treated with FAC or Ferr-1 or DFO. Significance was calculated using one-way ANOVA. The asterisks (*, **, ***) indicate significant differences at the P < 0.05, 0.01, 0.001 levels.

Figure 3

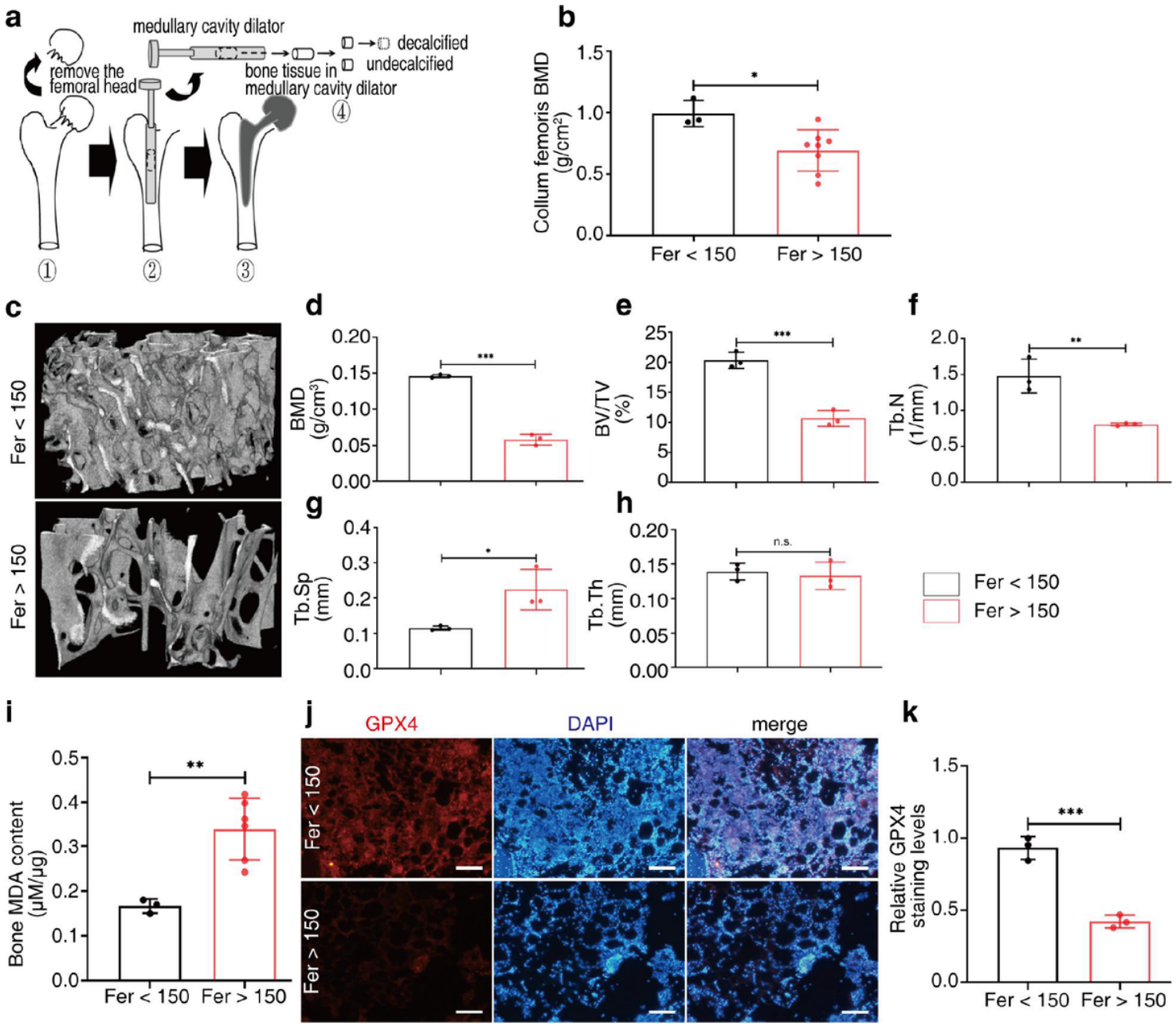

Figure 3

Excess-iron-induced osteoporosis involveds ferroptosis. (a) Schematic illustrating bone sample collection from patients during surgery. ① A femoral neck fracture in a patient, ② expanding the medullary cavity after removing the femoral head, ③ femoral head replacement, ④ removing bone tissue from the medullary cavity dilator, and dividing this into decalcified and undecalcified two parts. **(b)** Dual-energy X-ray absorptiometry to determine the collum femoris bone mineral density of 11 women with normal iron (serum ferritin < 150, μg/L, n = 3 biologically independent human samples) or iron accumulation (serum ferritin > 150 μg/L, n = 8 biologically independent human samples). Micro-CT to evaluate human bone microarchitecture. **(c)** Representative Micro-CT reconstructed three-dimensional images of human trabecular bone. **(d-h)** Micro-CT quantification of the trabecular bone index of human bone samples (n = 3 biologically independent human samples). The parameters examined included (**d**) BMD, (**e**) BV/TV, (**f**) Tb.N, **(g**) trabecular space (Tb.Sp), and (**h**) trabecular thickness (Tb.Th). **(i)** MDA content was measured in the undecalcified bone tissue of 11 women. **(j)** Immunofluorescence of decalcified bone tissue (frozen sections) stained against GPX4 (red) and DAPI (blue). Scale bar, 200 μm. **(k)** Quantification of GPX4 staining levels in the homans as shown in **j** (n = 3 biologically independent human samples). Student's t-tests were performed to determine assess differences. The asterisks (*, **, ***) indicate significant differences at the $P < 0.05$, 0.01, 0.001 levels.

Figure 4

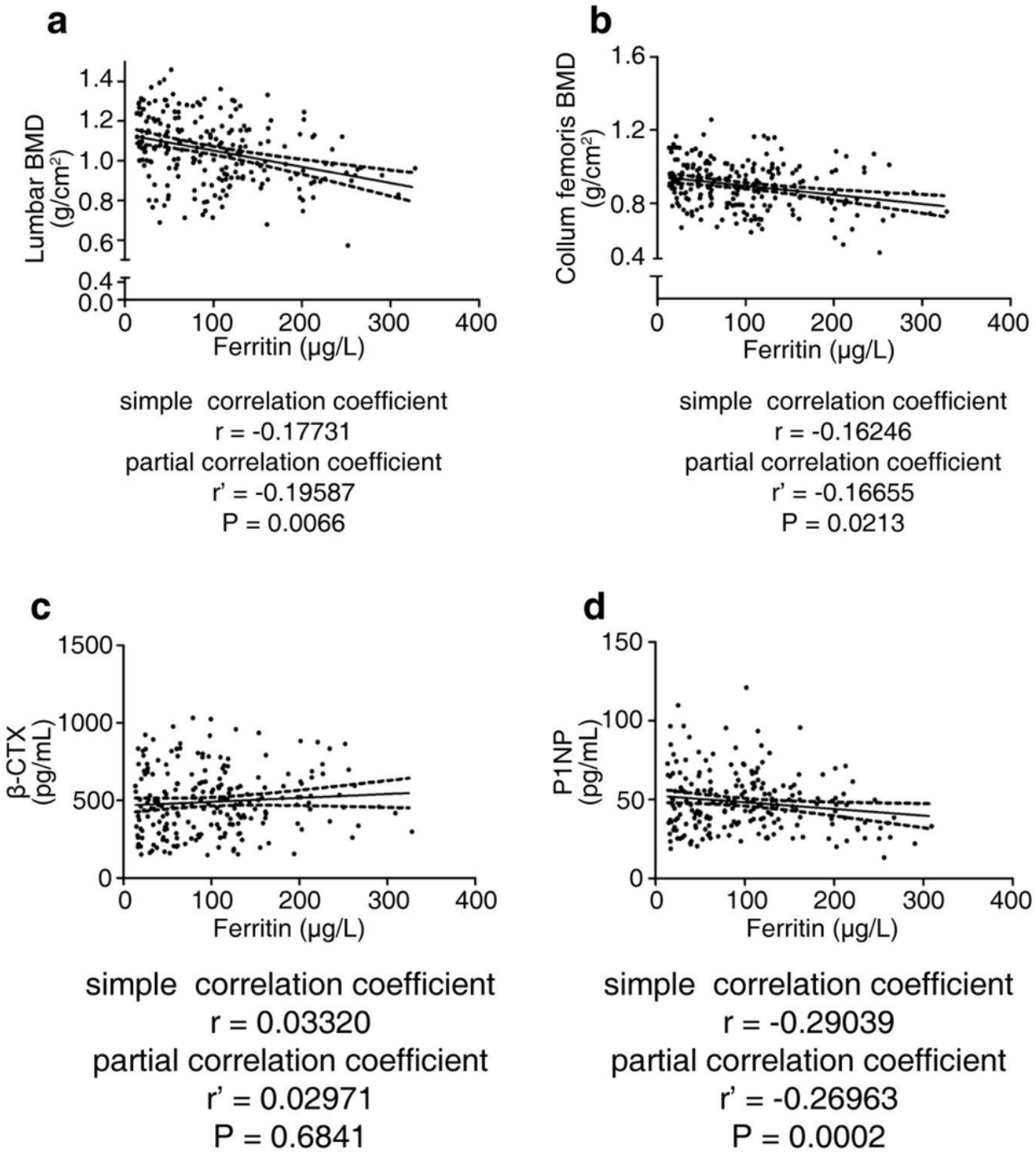

Figure 4

Data analysis of female physical examination. Multiple linear regression analysis to investigate the correlation between the ferritin level and **(a)** lumbar BMD, **(b)** collum femoris BMD, **(c)** bone resorption activity indicator β-cross-linked C-telopeptide of type I collagen (β-CTX), and **(d)** bone formation biomarker procollagen type 1 N-terminal propeptide (P1NP). n = 214. The simple correlation coefficients

(r) do not control for other variables, and the partial correlation coefficients (r') control for other variables shown in Supplementary Table 1 to exclude their influence.

Figure 5

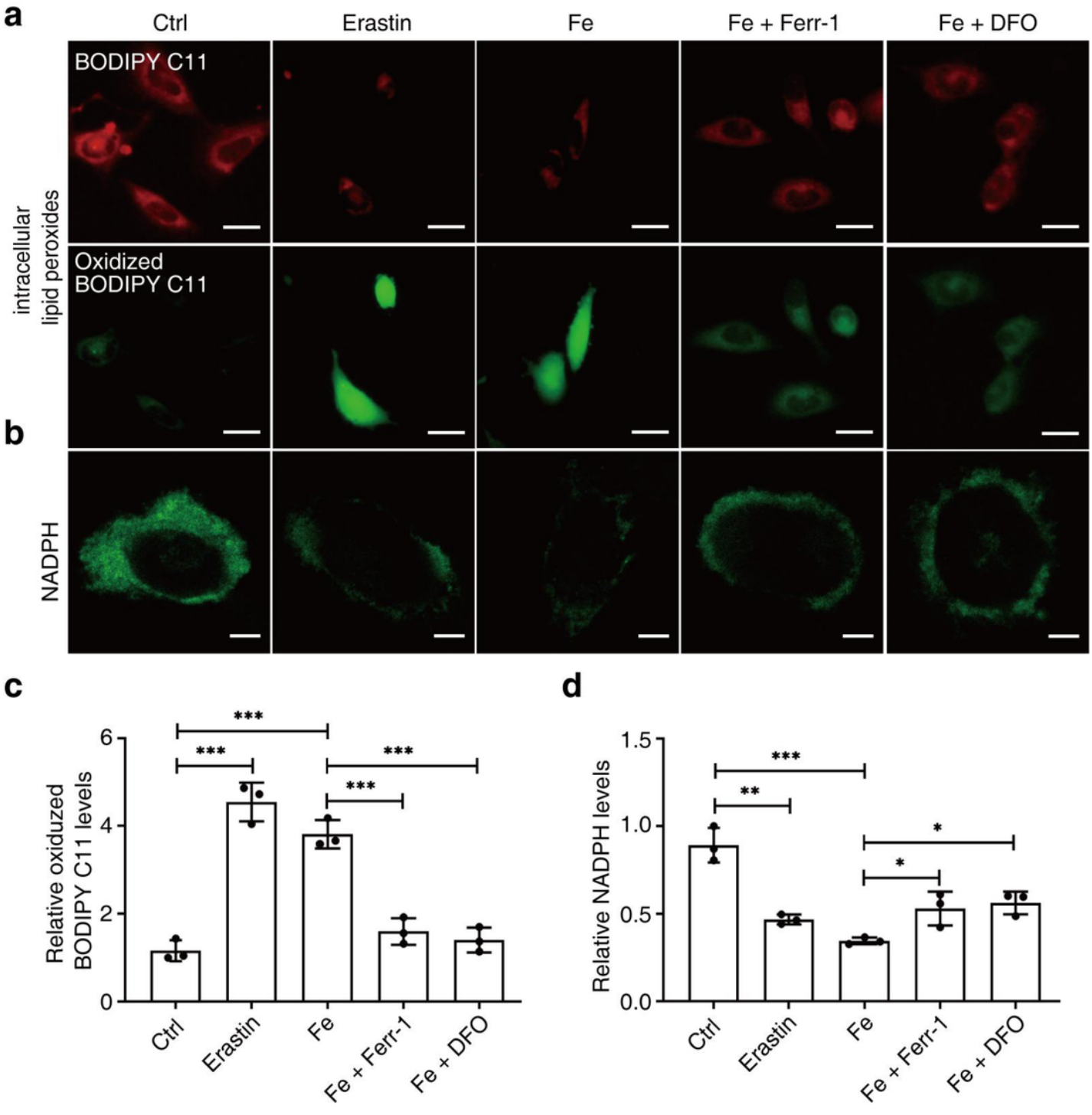

Figure 5

Characteristic appearances of excess-iron-induced ferroptosis in osteoblasts. (a) The intracellular lipid peroxide content was measured using BODIPY 581/591 C11 staining. Upper, the reduced lipid peroxide

sensor BODIPY 581/591 C11 emits red fluorescence, lower, oxidized BODIPY 581/591 C11 emits green fluorescence (n = 3 biologically independent cell samples). Scale bar, 20 μm. **(b)** The nicotinamide adenine dinucleotide phosphate (NADPH) level was measured using the iNap1 sensor (green) (n = 3biologically independent cell samples). Scale bar, 10 μm. **(c)** Quantification of lipid peroxide levels (lower) in the osteoblasts shown in **a** (n = 3 biologically independent cell samples). **(d)** Quantification of NADPH in the osteoblasts shown in **b** (n = 3 biologically independent cell samples). Osteoblasts were treated with either DMSO (Ctrl) or erastin or iron dextran (Fe) and/or Ferr-1 and/or deferoxamine (DFO). Significance in (**c** and **d**) was calculated using a one-way ANOVA. The asterisks (*, **, ***) indicate significant differences at the $P < 0.05$, 0.01, 0.001 levels.

Figure 6

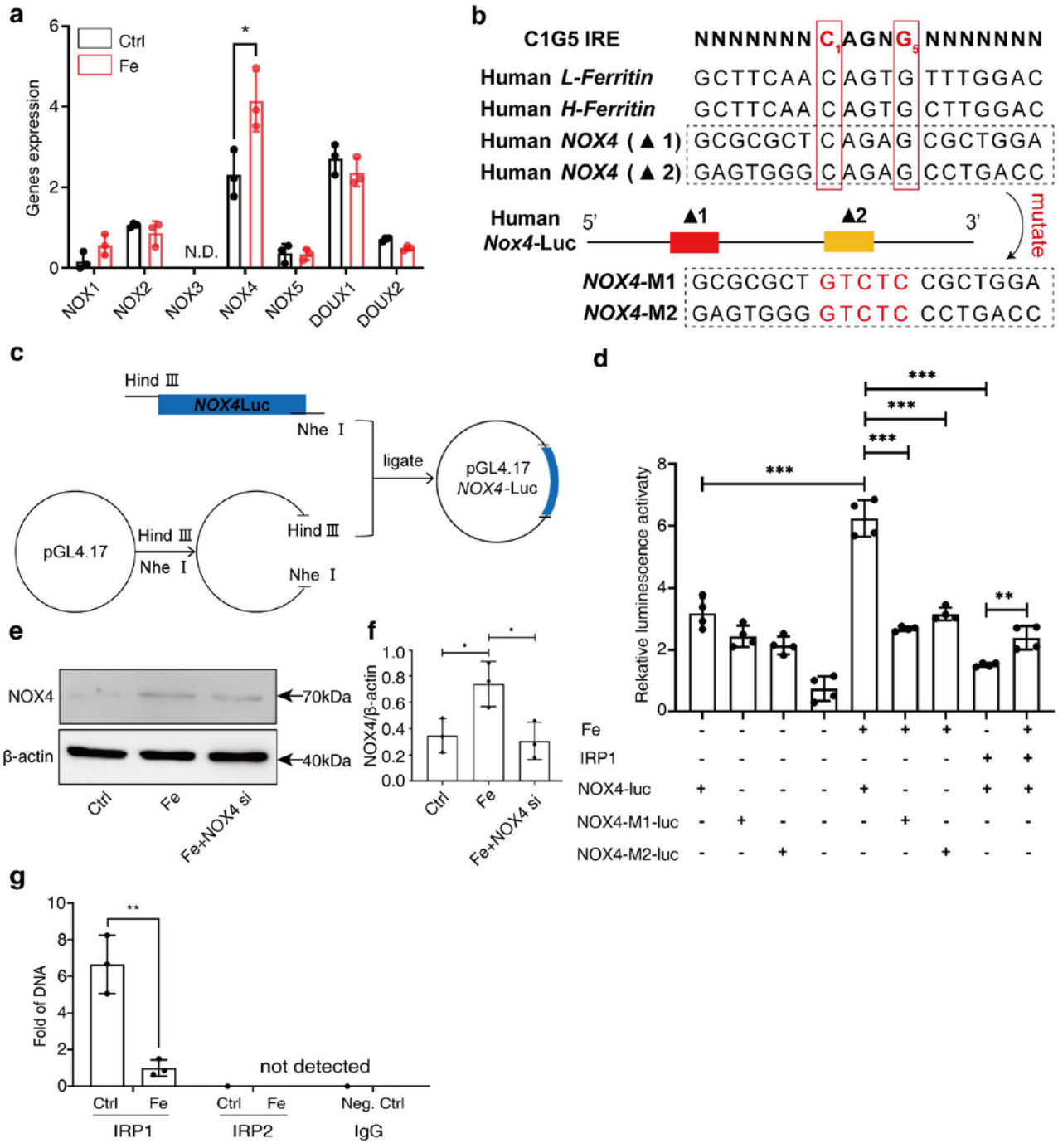

Figure 6

Iron binding causes dissociation of IRP1 from IRE-like sequences at the *NOX4* promoter to drive *NOX4* transcription. (a) *NOX*s (*NOX1-5*, *DOUX1*,*2*) mRNA was measured in osteoblasts treated with or without Fe. (n = 3 biologically independent cell samples). **(b)** Left, the sequences upstream regulatory region of the *NOX4* locus contains two sequences that are similar to previously characterized iron-response elements (IRE) present at ferritin high (H) and low (L) chain. Right, mutations within the first five

nucleotides according to the base complementary rule. **(c)** The sequences of human *NOX4* (NOX4-luc) was PCR amplified from hFOB1.19 osteoblasts. The forward and reverse primers were designed to incorporate Hind III, Nhe I restriction sites. PCR products were purified and ligated into the pGL4.17 vector using Hind III and Nhe I restriction sites. **(d)** Cells of the SaOS-2 human osteoblast cell line, cultured with or without Fe, co-transfected with IRP1 or NOX4-luc/NOX4-M1-luc/NOX4-M2-luc firefly and Renilla luciferase expression plasmids. Detected reporter activities were normalized to the levels for cells transfected with only the Renilla luciferase expression plasmid (n = 4 biologically independent cell samples). **(e)** Immunoblotting of NOX4 protein levels in hFOB1.19 cells treated with or without Fe. **(f)** Quantitation of the NOX4 band intensity from (e), protein levels were normalized to β-actin. **(g)** Cleavage Under Targets and Tagmentation (CUT&Tag) assays to assess the IRE-like-binding abilities of IRP1/IRP2 (n = 3 biologically independent cell samples). Significance in (**d**) was calculated using a one-way ANOVA, a Students t-test was used for (**a** and **g**). The asterisks (*, **, ***) indicate significant differences at the $P < 0.01$, 0.001 levels. N.D. not detected.

Figure 7

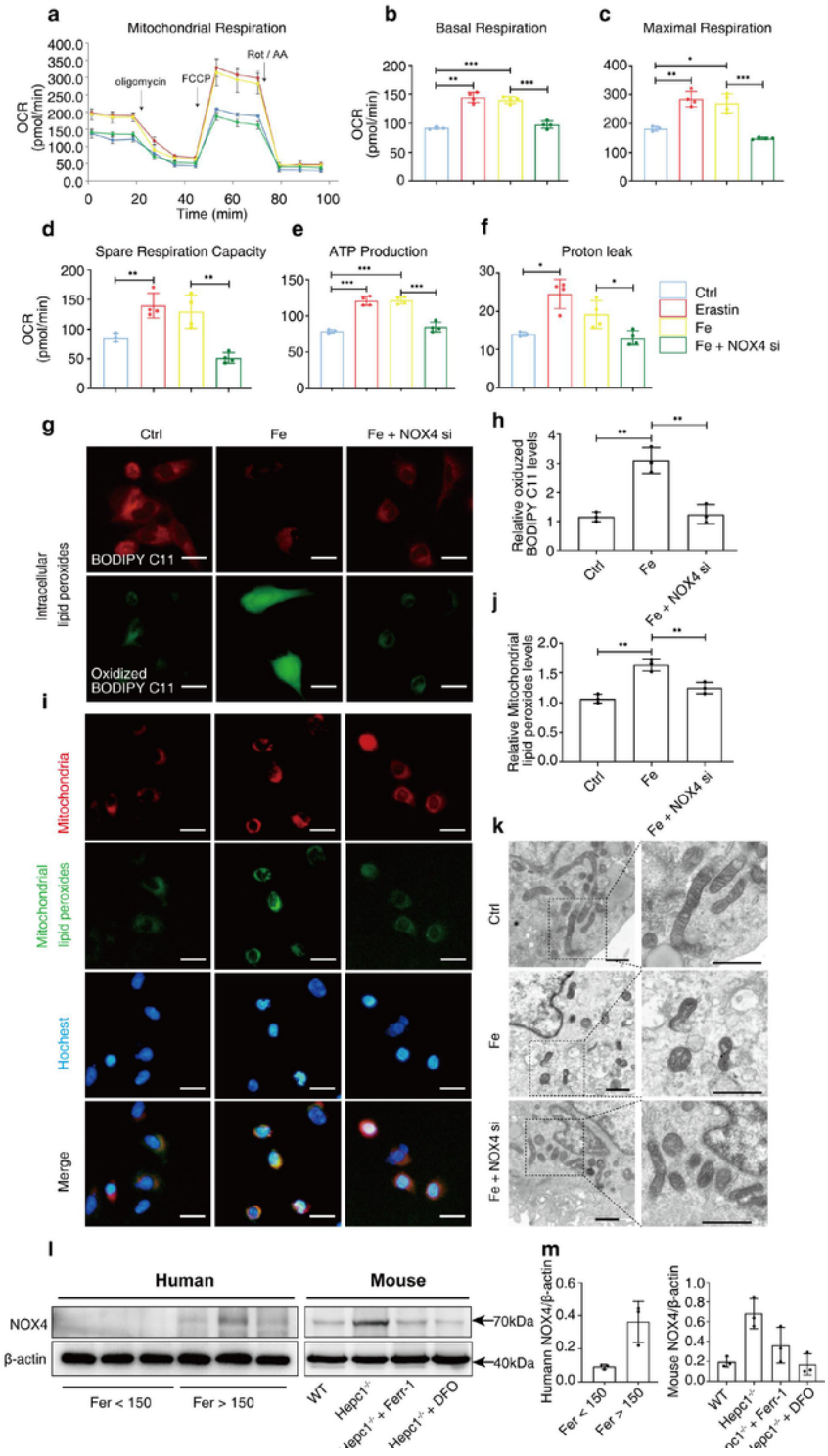

Figure 7

NOX4 mediates the ferroptosis of iron accumulating osteoblasts by activating mitochondria. (a) Whole-cell OCR of hFOB1.19 osteoblasts measured with a Seahorse instrument. Arrows indicate the timing for addition of oligomycin, FCCP, and rotenone/antimycin A (Rot/AA) (n = 3 or 4 biologically independent cell samples). **(b-f)** Quantitative analysis of (**b**) basal respiration, (**c**) maximum respiration, (**d**) spare respiration capacity, (**e**) ATP production, and (**f**) proton leakage of hFOB1.19 osteoblasts. **(g)** Intracellular

lipid peroxide levels measured using BODIPY 581/591 C11 staining (n = 3 biologically independent cell samples). Scale bar, 20 μm. **(h)** Quantification of lipid peroxides levels (lower) in the osteoblasts shown in **g** (n = 3 biologically independent cell samples). **(i)** Mitochondrial lipid peroxide levels measured using MitoPeDPP staining (n = 3 biologically independent cell samples). Scale bar, 20 μm. **(j)** Quantification of lipid peroxides levels in the osteoblasts mitochondria shown in **i** (n = 3 biologically independent cell samples). **(k)** Transmission electron microscopy (TEM) analysis of mitochondria in SaOS-2 osteoblasts. Upper, low-magnification view (×7000) of an osteoblast mitochondrion, lower, high-magnification view (×15000) of an osteoblast mitochondrion. Scale bar, 1 μm. **(l)** Immunoblotting of NOX4 protein levels in humans and mice. **(m)** Quantitation of the NOX4 band intensity from (**l**), protein levels were normalized to β-actin. Significance in (**b-f, h-j** and **m** right) was calculated using a one-way ANOVA (Student's t-tests was used in (**m**) left). The asterisks (*, **, ***) indicate significant differences at the P < 0.05, 0.01, 0.001 levels.

Supplementary Files

This is a list of supplementary files associated with this preprint. Click to download.

- Graphicalabstract.png
- SupplementaryInformation.pdf